Materials Today Advances 5 (2020) 100038

Contents lists available at ScienceDirect

Materials Today Advances

journal homepage: www.journals.elsevier.com/materials-today-advances/

Two-dimensional materials and metal-organic frameworks for the CO_2 reduction reaction

Mahider Asmare Tekalgne [a, e], H.H. Do [a, e], A. Hasani [a], Q. Van Le [b], H.W. Jang [c], S.H. Ahn [a, **], S.Y. Kim [d, *]

[a] School of Chemical Engineering and Materials Science, Chung-Ang University, 84 Heukseok-ro, Dongjak-gu, Seoul, 06974, Republic of Korea
[b] Institute of Research and Development, Duy Tan University, Da Nang, 550000, Viet Nam
[c] Department of Materials Science and Engineering, Research Institute of Advanced Materials, Seoul National University, Seoul, Republic of Korea
[d] Department of Materials Science and Engineering, Korea University, 145 Anam-ro, Seongbuk-gu, Seoul, 02841, Republic of Korea

ARTICLE INFO

Article history:
Received 9 August 2019
Received in revised form
12 November 2019
Accepted 19 November 2019
Available online xxx

Keywords:
Two dimensional materials
Metal-organic frameworks
CO_2 reduction
Electrochemical reduction
Photoelectrochemical reduction

ABSTRACT

The use of noble-free materials to convert atmospheric CO_2 into energy-rich fuels has gained a significant amount of attention in an effort toward decreasing global warming due to high concentrations of CO_2. Metallic catalysts, two-dimensional materials (such as graphene and graphene based), metal oxides, and metal-organic frameworks have been used as catalysts in the CO_2 reduction reaction and recently recognized as promising platforms due to their excellent electrical and thermal conductivity, outstanding mechanical properties, and good chemical stability. This review summarizes the progress made related to the electrochemical and photoelectrochemical CO_2 reduction reaction over the past few decades. In addition, the fundamentals and principles that govern both electrocatalytic and photocatalytic CO_2 reduction are discussed. Then, a detailed discussion of the different electrocatalysts, photocatalysts, and strategies used to improve the performance is provided.

1. Introduction

Not surprisingly, the emission of carbon dioxide (CO_2) is one of the greatest issues facing our lives today. CO_2 is the main component causing the greenhouse effect, leading to global warming and climate change [1,2]. Thus, the development of carbon capture and storage (CCS) technologies plays an important role in dealing with this problem [3–5]. However, the cost of CO_2 transport and selection of suitable storage sites for abundant volumes of CO_2 are significant challenges [6]. It is essential that the transport and storage are carefully implemented to minimize the risk of leakage [7]. Another solution is to convert CO_2 using catalysis. This approach not only remediates the adverse effects of this greenhouse gas, but also creates valuable products, such as CH_3OH, CH_4, and C_2H_5OH, which can be used as alternative fuels [8–12]. Among the previously reported materials, two-dimensional (2D) materials such as graphene [13,14], transition metal dichalcogenides (TMDs) [15–17], and metal-organic frameworks (MOFs) are potential candidates to act as catalysts for the CO_2 conversion process [18–20].

The birth of 2D materials has opened up a new era in the history of materials science and technology [21]. In particular, graphene is known as the first 2D material and is a hot research topic for scientists around the world, which led to Geim and Novoselov winning the Nobel Prize for physics in 2010 [22,23]. Abundant papers on graphene have been published in many famous journals in various fields such as chemistry [24,25], physics [26,27], and biology [28]. Due to its unique electronic, optical, and mechanical characteristics, graphene has been explored in various applications such as light-emitting diodes (LEDs), transistors, photodetectors, sensors, and solar cells [29–34]. Nevertheless, graphene does not have a band gap [35], which restricts its use in photocatalytic applications due to its low photo-absorption capacity. However, this can be overcome by using many approaches such as functionalization, doping, or applying a magnetic field [36–39]. Recently, Pablo Jarillo-Herrero's group at the Massachusetts Institute of Technology (MIT) in Cambridge created the magic-angle in graphene superlattices, which leads to unconventional superconductivity [40]. Twisted graphene was formed by stacking monolayer

* Corresponding author.
** Corresponding author.
E-mail addresses: shahn@cau.ac.kr (S.H. Ahn), sooyoungkim@korea.ac.kr (S.Y. Kim).
[e] M. Tekalgne and H. H. Do contributed equally to this work.

https://doi.org/10.1016/j.mtadv.2019.100038

graphene on top of another monolayer graphene rotated at an angle of ~1.1° to change its electronic properties. This material shows a flat band with approximately zero Fermi energy. Moreover, the resistance can be adjusted to zero at a critical temperature of up to 1.7 K. Therefore, twisted graphene has inspired scientists over the world and can be used for catalytic materials in the future.

Another group of 2D materials is TMDs, which were expected to create a breakthrough in catalytic applications. The molecular formula of TMDs is MX_2, where M is a transition metal (i.e., Mo, W, Nb …) and X is a chalcogen (S, Se, or Te) [41]. Typically, TMDs exist in a bulk phase made up of X-M-X layers held together via van der Waals (vdW) interactions [42,43]. Therefore, like graphene, TMDs nanosheets can be generated using various methods, such as mechanical exfoliation [44], chemical exfoliation, or chemical vapor deposition (CVD) [45,46]. When compared to bulk TMDs, TMD nanolayers have unique electronic and chemical features [47]. As a case in point, MoS_2 nanolayers have a direct band gap of 1.88 eV, which is suitable for electronic applications such as photovoltaic devices, biosensors, and transistors, while the indirect band gap for its bulk counterpart is 1.2 eV [48]. This can be explained based on the fact that the transition from indirect bandgap to direct bandgap of MoS_2 is due to the thickness reducing from bulk to monolayer. TMD materials are not only studied for electronic utilization, but also investigated in the field of catalysis. Many studies have indicated that the catalytic activity is shown on the edges of TMDs due to their electron state being near the Fermi level, which makes them promising candidates for the hydrogen evolution reaction (HER) [49,50]. TMDs are not only good for HER but are also effective in CO_2 reduction. However, it is essential to find a suitable catalyst to achieve cost-effective CO_2 reduction with high efficiency and selectivity. For instance, Asadi et al. investigated MoS_2 in ionic solution [51]. The result showed that the MoS_2 has better performance compared to noble metals with high current density and low overpotential, because of the d-electron density and metallic character of the active edge site. In addition, Li and coworkers investigated amorphous MoS_2 on polyethylenimine-modified reduced graphene oxide (GO) for CO production with a faradaic efficiency (FE) of 85.1% at overpotential of 540 mV [52]. Moreover, WSe_2 NFs showed the best performance in catalyzing CO_2 reduction to CO [53], realizing a current density of 18.95 mA cm^{-2}, an FE toward CO of 24%, and a CO formation turnover frequency of 0.28/s at −0.164 V. Another unique property of TMDs is that they have large surface areas and can be easily deposited onto conductive substrates, which make them highly useful in energy storage applications including batteries and supercapacitors [54,55]. In addition, two-dimensional hexagonal boron nitride (2D-hBN) [56], borophene (2D boron) [57], silicene (2D silicon) [58], and germanene (2D germanium) [59] are also considered as potential materials that can be incorporated with graphene and TMDs to boost the effect of the 2D materials in particular applications.

In the early 1990s, MOFs were initially considered as a new class of cage-like porous materials [60]. Later, they were developed by Omar Yaghi's group [61]. Professor Omar Yaghi is considered as a forefather in the field of MOF material research. Yaghi and his coworkers created a large number of MOF materials by designing structures based on reticular chemistry [62]. His group published the first work on MOF materials in 1999 reporting the development of MOF-5 [63]. This has been confirmed as the mostly clear evidence for the synthesis of an MOF by many chemists from around the world. To date, the discovery of MOFs has attracted a great deal of interest from researchers due to their outstanding properties such as large surface area, high thermal stability, high porosity, and diverse chemical components [64,65]. High surface area is the most impressive structural property of MOFs, helping them achieve a few records involving their surface area and hydrogen, methane, and CO_2 absorption capacity [66–69]. For instance, in 2012 a range of NU-110E materials set a record with Brunauer–Emmer–Teller (BET) surface areas of >7,000 (m^2/g) among porous materials including zeolites, covalent organic frameworks (COFs), zeolitic imidazolate frameworks (ZIFs), amorphous porous polymer, and active carbon [66]. Using a computational approach, scientists have demonstrated that MOF materials can achieve a maximum surface area of 14,600 m^2/g. In addition, MOF materials with high surface areas include UMCM-2 (5,200 m^2/g), NU-100 (6,140 m^2/g), and MOF-210 (6,240 m^2/g) [70–72]. The pore size of an MOF can be controlled by expanding the length of the organic linker or attaching substituents onto the organic linker [73]. These features help MOFs to exhibit good selective gas adsorption abilities. Moreover, two outstanding properties have enabled MOFs to become potential catalysts for CO_2 conversion. First, MOFs contain open metal sites (OMSs), operating as Lewis acid catalytic sites as seen in Cu-BTC, MIL-100, UiO-66, and so on [74–76]. Many MOFs with OMSs have been investigated for catalyzing certain reactions. For example, Snejko et al. synthesized a series of In-based MOFs to catalyze the acetalization of aldehydes [77]. The outcome revealed that MOFs endowed with OMSs exhibited higher activity than catalysts without OMSs. Second, functional groups on MOFs materials, including organic groups and inorganic groups can significantly enhance catalytic activity. For example, Fu et al. studied the performance of MIL-125(Ti) and NH_2-MIL-125(Ti) for CO_2 reduction reaction into $HCOO^-$ [78]. The result demonstrated that amino-modification of MIL-125(Ti) showed a reaction rate of 16.28 μmol/h/g while MIL-125(Ti) is not active.

Considering the significant growth of recent studies on 2D materials and MOFs for use in the CO_2 reduction reaction, this review summarizes the results obtained for 2D materials and MOFs in CO_2 reduction research, including the photocatalytic and electrocatalytic CO_2 reduction processes.

2. Fundamentals of electrocatalytic and photocatalytic CO_2 reduction reaction

Since CO_2 is one of the most stable molecules due to the presence of strong C=O double bonds, its multistep reduction via electrochemical or photochemical approaches is more demanding than the water splitting reaction and has many technical difficulties [79–81]. The reduction reaction may proceed via several different pathways yielding a diverse range of reduction products including methanol (CH_3OH), carbon monoxide (CO), formic acid (HCOOH), methane (CH_4), ethylene (C_2H_4), and others [82,83]. Thus, the overall design process for the CO_2 reduction reaction depends on the target product needed.

2.1. Electrocatalytic CO_2 reduction

Fundamental studies on the electrochemical reduction of CO_2 started in the early 19th century and have subsequently been conducted extensively. The electrocatalytic reduction of CO_2 is a promising strategy for transforming CO_2 into useful fuels. The electrocatalytic reduction of CO_2 consists of two half reactions (Fig. 1) that can occur via a two to fourteen-electron exchange process. These reactions are provided in Table 1 and are accompanied by a variety of standard electrode potentials (vs. the standard hydrogen electrode (SHE)) [2].

The first step to reduce CO_2 is the chemical conversion of CO_2 into reduced carbon species, which is a difficult process due to the poor and sluggish kinetics observed for the electroreduction of CO_2 [84–86]. In a typical single-electron CO_2 reduction process, the anode and cathode are placed in two chambers, where water is

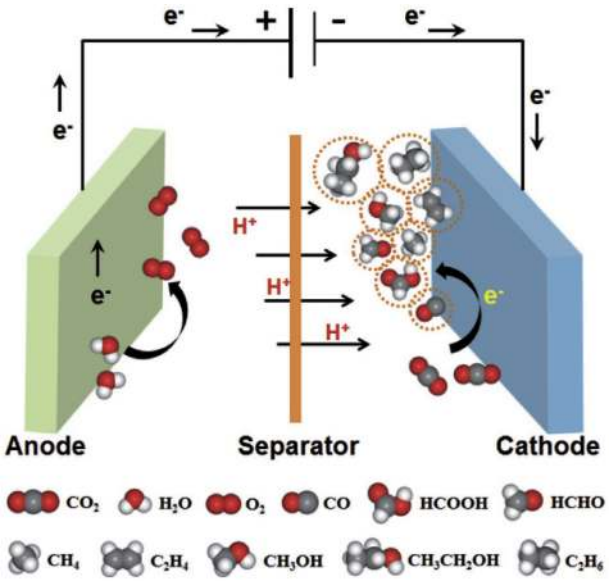

Fig. 1. An illustration of electrocatalysts for CO_2 reduction reaction and possible products created in an electrochemical cell. Reproduced with permission [217]; copyright 2018, WILEY-VCH.

Table 1
Standard electrochemical potentials for CO_2 reduction.

Reduction potentials of CO_2	Standard electrode potentials vs. SHE (V)
$CO_2 + 2H^+ + 2e^- \rightarrow CO + H_2O$	−0.106
$CO_2 + 2H^+ + 2e^- \rightarrow HCOOH + H_2O$	−0.250
$2CO_2 + 2H^+ + 2e^- \rightarrow H_2C_2O_4$	−0.500
$CO_2 + 4H^+ + 4e^- \rightarrow C + 2H_2O$	0.210
$CO_2 + 4H^+ + 4e^- \rightarrow CH_2O + 2H_2O$	−0.070
$CO_2 + 6H^+ + 6e^- \rightarrow CH_3OH + H_2O$	0.016
$CO_2 + 8H^+ + 8e^- \rightarrow CH_4 + 2H_2O$	0.169
$CO_2 + 12H^+ + 12e^- \rightarrow C_2H_4 + 4H_2O$	0.064
$CO_2 + 14H^+ + 14e^- \rightarrow C_2H_6 + 4H_2O$	0.084

oxidized to form molecular oxygen at the anode and CO_2 is reduced to form the reduced carbon species at the cathode. The thermodynamic potential to drive the one-electron reduction of CO_2 to form CO_2^- is −1.90 V vs. SHE in aqueous media at pH = 7, making the reaction highly energetic and unfavorable [87–89]. In the first step, the generation of CO_2^- is critical because it is the rate-limiting step and the coordination of this intermediate determines whether the $2e^-$ reduction product will either be CO or formate. However, multi-electron proton-assisted electron transfer processes are more favorable within the potential range of −0.2 to −0.6 V vs. SHE, leading to a wide range of CO_2^- derived products depending on the catalyst and electrolyte used [90–93]. Over the past few years, both aqueous and non-aqueous electrolytes have been studied in the CO_2 reduction reaction [84,94,95]. The most commonly used electrolyte is a 0.5 M $NaHCO_3$ (or $KHCO_3$) solution at pH 7, as it acts as a buffer to maintain the pH value at the electrode surface [84,96,97]. The pH value should be taken into consideration as it reduces the undesired HER. The selective production of desirable chemicals in this process is very challenging because of the similarity in the redox potentials for all the possible reaction pathways. Electrochemical CO_2 reduction occurs in a few steps.

The subsequent reduction steps take place almost instantaneously when compared to the first step. Therefore, stabilization of this high-energy intermediate is key to achieving a high rate and energy-efficient CO_2 reduction process. Metals such as Pb, Hg, In, Sn, Cd, and Tl do not bind to the CO_2 intermediate and cannot reduce CO. However, metals such as Au, Ag, Zn, and Ga bind to the CO_2 intermediate, but cannot reduce CO, whereas copper binds to the CO_2 intermediate and can reduce CO.

To date, almost all of the reported catalysts used in the CO_2 electroreduction reaction are inorganic materials such as metals, and semiconductors. For example, a series of metals were investigated by Hori et al. for the electrocatalytic conversion of CO_2 in water [97]. The study indicated that the $HCOO^-$ ion was created using metals such as Cd, Hg, In, Pb, Sn, and Tl as the working electrode. For the noble metal group containing Pt, Au, Ag, Cu, Pb, Ga, Ni, and Zn, CO_2 was electroreduced to form CO. The binding force between the metal surface and CO molecules plays a crucial role in the reduction of CO_2. A large value of the binding energy of metals and CO shows low performance.

There are some important parameters to assess electrocatalytic activity in the CO_2 reduction reaction [98]:

Onset potential: The onset potential is the working potential at which the current of the electrochemical reaction starts to change from the background. However, when contribution of capacity is remarkable, the determination of onset potential is more difficult. Thus this value is not a clear parameter to evaluate catalytic activity in the experiment.

Tafel slope: The Tafel slope can be calculated by fitting the linear region of the curve of the Tafel equation ($\eta = b \log j + a$) where, η overpotential, b: Tafel slope, and j: current density. If the Tafel slope is small, it implies that the sharp rise in the current density with the escalating overpotential occurs in an electrochemical reaction. In addition, it is also a requirement for good electrocatalysts.

Turnover frequency: TOF is a measure of per-site activity of catalysts at a certain overpotential. It reflects the intrinsic activity of an electrocatalyst and allows the comparison among different materials regardless of their actual geometric parameters or areal loading [99]. However, it is difficult to be calculated due to the difficulty in precisely knowing the active sites available in the catalyst.

Faradaic efficiency: FE of a specific product is described as the fraction of charges transferred to this product and the total charges in the electrochemical process. A material with FE higher than 80% is considered as a good catalyst for the CO_2 reduction reaction.

Stability: To evaluate the stability of the electrocatalysts, the cyclic voltammetry method is usually applied in the electrocatalytic reaction. If the catalyst is durable over a long time, it can be utilized in the industrial application.

2.2. Photocatalytic CO_2 reduction reaction

The photoreduction of CO_2 occurs under both UV and visible light irradiation. Depending on their different potentials, the products of the CO_2 reduction process can include CO, HCHO, CH_3OH, and CH_4. Table 2 gives the reduction potentials for the CO_2

Table 2
Standard photoreduction potentials for CO_2 reduction.

Reduction potentials of CO_2	Reduction potential vs. NHE (V)
$CO_2 + e^- \rightarrow CO_2^-$	−1.9
$CO_2 + 2H^+ + 2e^- \rightarrow HCOOH$	−0.61
$CO_2 + 2H^+ + 2e^- \rightarrow CO + H_2O$	−0.53
$CO_2 + 2H^+ + 2e^- \rightarrow HCOO^-$	−0.49
$CO_2 + 4H^+ + 4e^- \rightarrow HCHO + H_2O$	−0.48
$2H^+ + 2e^- \rightarrow H_2$	−0.41
$CO_2 + 6H^+ + 6e^- \rightarrow CH_3OH + H_2O$	−0.38
$CO_2 + 8H^+ + 8e^- \rightarrow HCHO + H_2O$	−0.24
$H_2O \rightarrow 1/2O_2 + 2H^+ + 2e^-$	+0.41

reduction process. In particular, the photocatalytic CO_2 reduction process involves a series of reactions including CO_2 adsorption, electron–hole pair photogeneration, charge carrier separation, charge carrier transportation, and chemical reactions between the surface species and charge carriers [100,101]. However, not all the photoinduced electrons on the surface of the catalyst are utilized for the reduction of CO_2. Thus, catalysts with a relatively low band gap value and high redox potential are favorable. Similarly, the photoinduced activation of CO_2 on MOFs consists of some principal steps. The catalytic material adsorbs a photon leading to the separation of the electron–hole pairs, resulting in a negative electron (e^-) being excited from the highest occupied molecular orbital (HOMO) to the lowest unoccupied molecular orbital (LUMO) and simultaneously, a positive hole (h^+) is left on the HOMO. The CO_2 molecules are then absorbed on the catalytic centers of the MOFs and accept electrons to form different products such as CO, CH_4, and HCOOH. The mechanism of the CO_2 reduction process on an inorganic semiconductor and MOFs is shown in Fig. 2 and Fig. 3. Nevertheless, not all MOFs exhibit photocatalytic activity and their electronic properties are not identical. This may be determined based on the HOMO and LUMO of MOF materials.

The HOMO level energy of MOFs normally represents the organic ligands, while the relationship between the reduction potential of the metal clusters and LUMO level energy of the MOFs has been demonstrated. Besides, several studies have indicated that the organic linkers play a more important role than the metal nodes toward influencing the electronic characteristics. Therefore, researchers should use these elements to find an ideal photocatalyst for the CO_2 reduction reaction. The LUMO level energy of an MOF material is more negative than the redox potential for CO_2 conversion. For example, PCN-222 has an LUMO of −0.4 V and is therefore appropriate for converting CO_2 into CH_4 and CH_3OH because the reduction potentials of CO_2 into methane and methanol are −0.24 and −0.38 V, respectively. In addition, the photon-absorption ability is also one of the most important factor that affects the features of photoactive MOFs. This capacity relies on electron-rich organic ligands and can be adjusted using the HUMO and LUMO gap width by attaching functional groups onto the organic linker or modifying the metal centers in the MOF.

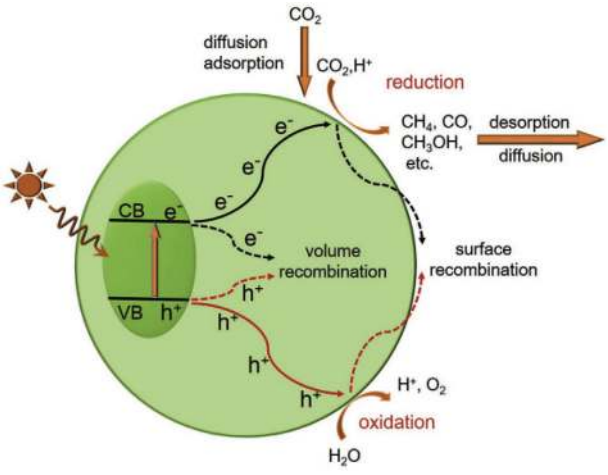

Fig. 2. An illustration of photocatalysts for CO_2 reduction reaction. Reproduced with permission [98]; copyright 2018, WILEY-VCH.

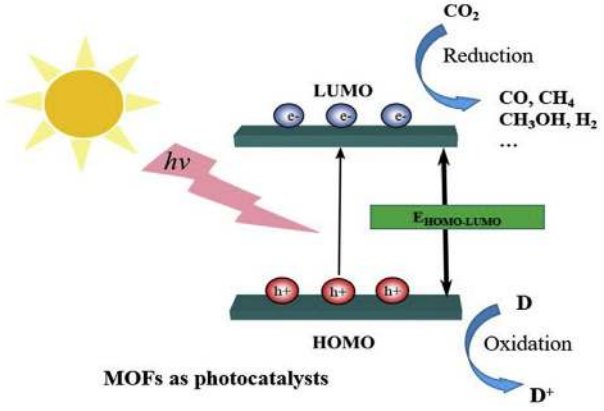

Fig. 3. Illustration of MOFs used for the photocatalytic reduction of CO_2 (D: an electron donor).

3. Materials used as efficient electrocatalysts in the CO_2 reduction reaction

The existing electrocatalysts used in CO_2 reduction reaction can be categorized into the following groups: metallic, metal chalcogenides, metal oxides, nitrogen containing carbon materials, and molecular catalysts [84,102–107]. For the metallic catalysts, the product distribution of the CO_2 reduction reaction varies widely, primarily depending on the electrode metals and electrolyte used. The electrode provides the site of the reaction and the product selectivity in the CO_2 reduction reaction is affected by whether or not the reactants and other related species are adsorbed. CO_2 can be reduced into different products based on the metal used. For example, metals such as Au, Ag, and Zn produce CO, while metals such as Sn, In, and Pb selectively form formate as their primary product. Catalysts beyond metals such as non-metallic materials [108–110], bi-metallics, metal chalcogenides, and MOFs have also been recently studied as promising catalysts in the CO_2 reduction reaction. The different types of electrocatalysts used in the CO_2 reduction reaction will be discussed in the following sections.

3.1. Metallic catalysts

Elemental metals are among the earliest electrocatalysts investigated in the CO_2 reduction reaction, which date back to the early 1980s, where the catalytic activity of bulk metal catalysts was studied [111–114]. However, the products obtained were dependent on many factors such as the materials used as the cathode, the electrolyte, and operating conditions (such as pressure and temperature) [115,116]. The pure metal electrocatalysts used in the CO_2 reduction reaction are generally categorized into different groups. CO is the major product on metals such as Au, Ag, Zn, Pd, and Ga because they can bind the $CO_2^{\bullet-}$ intermediate, catalyze the cleavage of the C–O bond, and allow the CO product to be easily desorbed from the electrode. On the contrary, metals such as Sn, Pb, Bi, and In hardly adsorb $CO_2^{\bullet-}$ and the carbon atom is protonated and ultimately transformed into formate or formic acid as a major product. Metals such as Pt, Ni, Ti, and Fe form H_2 as their major product because of their low HER overpotential and strong CO adsorption. In addition, studies have shown that Cu is the only elemental metal to produce C_1–C_3 hydrocarbons via COH or CHO intermediates [117].

During the electrocatalytic CO_2 reduction reaction, the morphology, roughness, and size of the catalyst used have an immense influence on the activity and product selectivity [90,102,118]. Thus, numerous studies on how to improve these catalysts have been reported and are currently under progress.

Due to its high surface area and large number of active sites, the size of the metal has been found to play an important role in the

selectivity and activity observed in the CO_2 reduction reaction [119,120]. Nanostructured electrocatalysts generally have a larger number of surface active sites than their bulk materials and exhibit improved tolerance to impurities in electrolytes with improved selectivity, and enhanced stability. Thus, the impact it has on the CO_2 reduction process has been investigated both theoretically and experimentally for some metals such as Cu, Ag, and Au [120,121]. For example, Mistry et al. investigated the size-dependent activity enhancement in the electroreduction of CO_2 over Au nanoparticles (NPs) [122]. They investigated the catalytic activity of Au NPs for production of CO in the size range of 1–8 nm in 0.1 M $KHCO_3$.

An increase in the current density was observed upon decreasing the particle size, along with a decrease in the Faradaic selectivity toward CO. Moreover, in another study looking at the catalyst-structure effect, Au islands were prepared via oxygen plasma treatment on Au foil to increase the current density for the selective production of carbon monoxide with >95% FE [123]. The FE, product formation rate, and onset potential for CO_2 reduction were all improved due to the expanded surface area when compared to a polycrystalline Au electrode. The CO_2 reduction performance was further enhanced upon the addition of an ionic liquid (1-butyl-3-methylimidazolium tetrafluoroborate) to the electrolyte, which increased the CO_2 solubility and decreased the CO_2 reduction overpotential (Fig. 4).

Similarly, for Cu metal, Strasser and co-workers discovered that Cu NPs exhibited an enhanced total current density and higher selectivity toward CO and H_2 upon decreasing the particle size, particularly for those under 5 nm, while the hydrocarbon selectivity was increasingly suppressed [120]. DFT calculations indicate this phenomenon was related to the higher density of low-coordinated sites on the small nanoparticles, which promoted the HER over CO_2 reduction to form CO. Furthermore, a similar trend was observed for Ag NPs. However, in this case the CO_2 reduction current density first increased as the size of the NPs decreased until 5 nm and then decreased again with particles sizes <5 nm. This showed that optimization of the particle size is also another important parameter to consider [124]. In another study, Hsieh et al. reported a 'nano-coral' structured Ag catalyst prepared via an oxidation–reduction method. This structure shows higher performance than bulk Ag with a 95% FE toward CO at a low overpotential of 0.37 V and a current density of 2 mA cm^{-2}. Furthermore, the nanoporous structure was also used for Au to achieve an improved performance in the CO_2 reduction reaction to form CO. Hall et al. reported ordered Au inverse opal (Au-IO) thin films with a series of thicknesses using a templating process with 200 nm polystyrene spheres [125]. The resulting Au-IO electrodes exhibited high specific performance, which was inversely proportional to the film thickness due to the difficult mass transportation observed in the thicker electrodes.

In addition to the particle size, surface roughening is also an effective strategy to increase the surface area and promote the CO_2 reduction reaction performance. Tang et al. investigated the importance of the surface morphology of Cu in the CO_2 reduction reaction [126]. In this study, the copper nanoparticle covered electrode showed an increased selectivity toward hydrocarbons when compared to an electropolished copper electrode surface and argon sputtered copper electrode. The enhanced performance was attributed to the increase in the surface area and the generation of active sites such as edges and defects, which have lower energy barriers for the formation of the CO_2 reduction reaction intermediates.

Another parameter in the CO_2 reduction reaction is the choice of electrolyte. The solvent and pH control the concentration of the reactants, CO_2 and H^*. Furthermore, the solvent, pH, and presence of certain cations and anions can stabilize the reaction intermediates or inhibit the reduction of CO_2 [127]. Many studies have been conducted to investigate the role of anions and cations in the electrolyte [111,128]. For example, Hori and Murata reported the

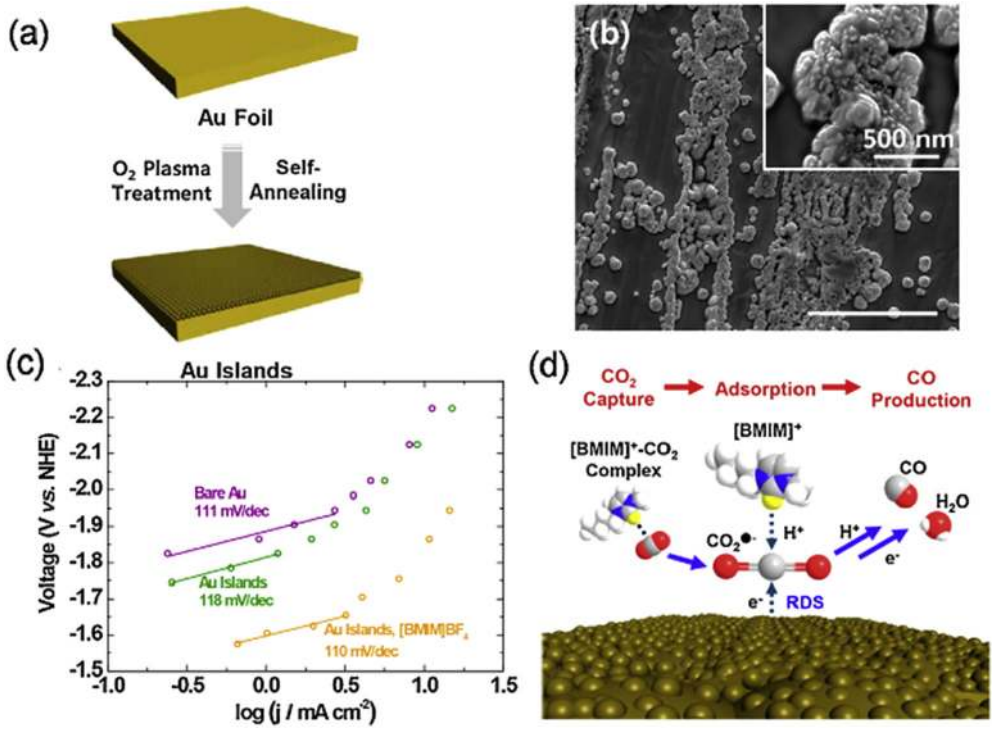

Fig. 4. CO_2 reduction on Au islands: (a) a schematic illustration of the Au island formation process, (b) SEM image, (c) Tafel plot, and (d) schematic representation of CO_2 reduction on the catalyst surface of Au islands with an ionic liquid electrolyte. Reproduced with permission [123]; copyright 2015, American Chemical Society.

prevention of the HER using different alkaline cations and obtained the highest selectivity toward hydrocarbons using K^+ [111]. Furthermore, Kyriacou et al. have recently shown that the rate of reduction can be influenced using multivalent cations as the supporting electrolyte [128]. However, further studies to understand the role of cations and anions are needed because they have an effect on the catalyst's reactivity and selectivity.

Another method to improve the efficiency of a metal electrocatalyst is the oxidation and reduction of the metallic electrodes to create active surface sites for the CO_2 reduction reaction. This phenomenon was first reported by Frese, in which an oxidized and in situ reduced Cu electrode used during the CO_2 reduction reaction showed improved methanol production when compared to an untreated polycrystalline Cu electrode [129]. Later, Li and Kanan applied this method to study the correlation between the oxidation temperature and activity [130]. The highest activity was achieved after thermal treatment at 500 °C for 12 h in the air and the resulting Cu electrode formed a nanowire structure with a coarse surface during the in situ reduction of CO_2. Similarly, a bulk Sn metal electrode requires a large overpotential (>0.86 V) in order to generate a moderate current density (5 mA cm^{-2}) in the CO_2 reduction reaction to form formic acid with an FE of 88.4% [131]. In another study, Kanan and co-workers compared the activity of a Sn electrode bearing a native SnO_x layer and an electrode etched to expose the metallic Sn^0 surface [132]. It was proposed that SnO_x directly participated in the CO_2 reduction pathway by stabilizing the $CO_2^{\bullet-}$ intermediate because the electron transfer to CO_2 was excessively slow on metallic Sn (Fig. 5a and b). In addition, Xie and co-workers recently showed that metallic Sn quantum sheets confined in graphene display a large current density of 21.1 mA cm^{-2}, FE of ~90%, and great stability for over 50 h at −1.8 V vs. a saturated calomel electrode (SCE) during the selective CO_2 reduction reaction to form formate (Fig. 5d–g) [133]. Moreover, Zhou and co-workers discovered the dependence of the selectivity in the CO_2 reduction reaction on the surface thickness of the SnO_x layer. They found that an SnO_x electrode with a surface thickness of ~3.5 nm displayed the maximum FE of 64% for formate, and a FE of 35% for CO was achieved using a SnO_x layer thickness of 7.0 nm [134].

3.2. Graphene and graphene-based hybrid catalysts

Due to their unique structural and electronic properties, 2D catalysts have been the main focus of several research studies [135]. As a substitute to the expensive and rare noble metals, 2D materials have large number of active sites that are useful for fast interfacial charge transfer and electrochemical catalysis [136]. Among them, graphene, a thin and single layered carbon material obtained from graphite and consisting of a honeycomb-like structure with unique physical and electronic properties [137], has gained a lot of attention over the past decade. Though carbon-based catalysts have been widely studied in the HER, they have rarely been investigated in the CO_2 reduction reaction. In addition, pure graphene and graphene-like carbon materials exhibit lower catalytic activities due to the negligible ability to adsorb and activate the CO_2 molecule as well as the very high free energy barrier for the elementary step of *COOH formation [136], while doping with heteroatoms, such as B, N, and/or Ni, can modify the structure of graphene and also decrease the CO_2 adsorption barrier and facilitate the electrocatalytic CO_2 reduction reaction. Studies have shown that doping boron stabilizes the negatively polarized O atoms of CO_2 enhancing the chemisorption of CO_2 onto the carbon surface [138]. Further, in graphene-based composites, graphene gives large surface areas excellent conductivity as a support for active phases such as NPs and nanosheets. The combination results in enhancement of charge transport to facilitate CO_2 conversion [139].

Rogers et al. reported the enhancement in the electrocatalytic CO_2 reduction reaction using gold nanoparticles (AuNP) embedded in a functional graphene nanoribbon composite electrode [140].

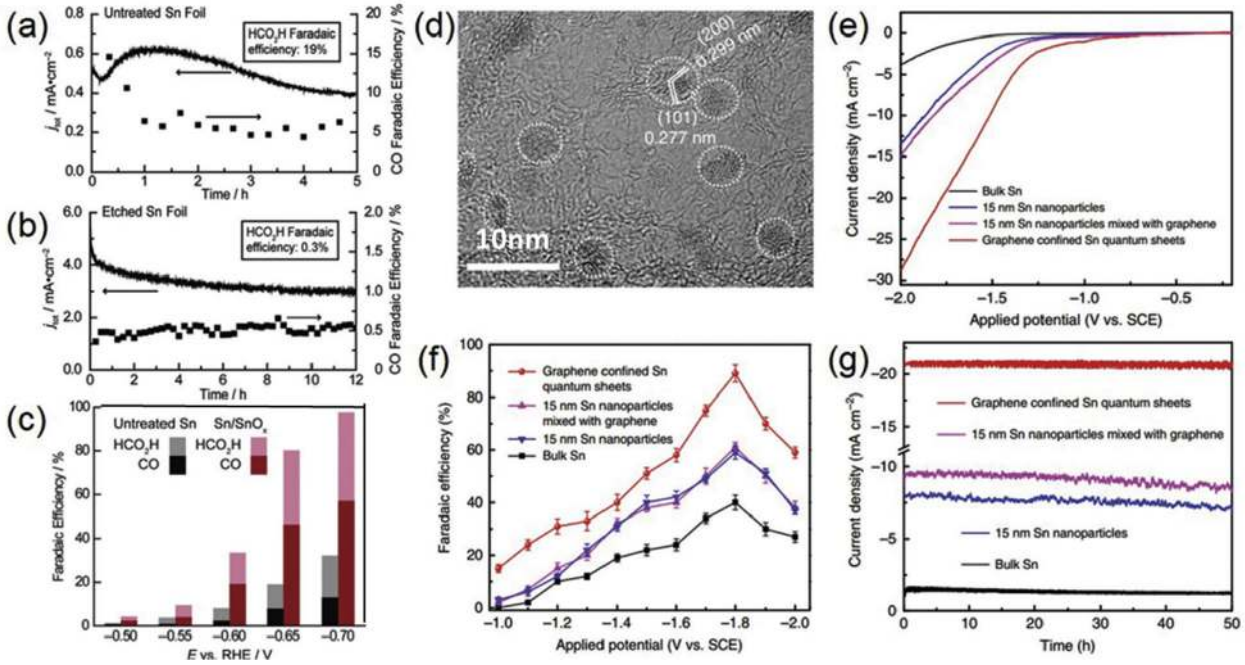

Fig. 5. Change in the total current density and CO Faradaic efficiency (FE) with time on: (a) untreated Sn,(b) Sn etched at −0.7 V vs. RHE in 0.5 M $NaHCO_3$, and (c) their potential-dependent FE for CO and formic acid. Reproduced with permission [127] Copyright 2012, American Chemistry Society. (d) High-magnification TEM image of Sn quantum sheets confined in graphene, (e) polarization curves, (f) potential-dependent FE for formate, and (g) chronoamperometry stability at −1.8 V versus SCE on Sn quantum sheets confined in graphene in a 0.1 M $NaHCO_3$ aqueous solution. Reproduced with permission [128;] copyright 2016, Nature Publishing Group.

This study revealed that the structural and electronic properties of the graphene nanoribbon composite matrix increased the active surface area of the AuNP, reduced the overpotential for CO_2 reduction (catalytic onset >−0.2 V vs. RHE), increased the FE to >90%, significantly improved stability of the catalyst, and increased the total catalytic output when compared to an amorphous carbon AuNP support. Furthermore, Su et al. investigated nickel-nitrogen-modified graphene as an efficient catalyst for the reduction of CO_2 to CO [141]. The modified graphene catalyst was successfully synthesized via a short-duration heat treatment of a Ni–N organometallic complex in the presence of GO. This heat treatment method enhanced the performance of the catalyst by introducing Ni and N atoms, which are active centers for the CO_2 reduction reaction, into the sp^2 networks of graphene.

Moreover, Li et al. reported a catalyst based on two-dimensional SnS_2 nanosheets supported on reduced GO (SnS_2/rGO) synthesized via a one-pot hydrothermal method used for the highly selective electrocatalytic reduction of CO_2 to form formate [142]. The catalyst was capable of producing formate at overpotentials as low as 0.23 V, and reaches a maximum FE of 84.5% and current density of 13.9 mA cm^{-2} at overpotential of 0.68 V in an aqueous bicarbonate solution. The electrocatalytic activity toward the CO_2 reduction reaction arises from the presence of reduced metallic tin formed from SnS_2 under cathodic electrolysis conditions.

3.3. Transition metal chalcogenides

TMDs such as MoS_2, $MoSe_2$, and WS_2 have been widely investigated as HER electrocatalysts [143]. However, they have recently been discovered as potential catalysts for the CO_2 reduction reaction. However, enhancing the current density at a low overpotential, slowing down the competitive HER, and improving the long-term stability are some of the challenges that need to be addressed. In addition, the CO_2 reduction process using TMDs should be carried out in a mixed solution consisting of an ionic liquid (such as EMIM-BF_4), which can form a stable complex with the $CO_2^{\bullet-}$ intermediate and water to suppress the HER. Moreover, a study by Nørskov and co-workers showed that the binding properties of CO_2 reduction intermediates such as COOH and CHO on the MoS_2 and $MoSe_2$ edges prefer bridging S or Se atoms, while CO was selectively adsorbed on the metal atom [144,145].

Asadi et al. compared the CO_2 reduction performance of four different TMD materials (MoS_2, $MoSe_2$, WS_2, and WSe_2) with similar sizes [53]. They found that WSe_2 nanoflakes were the most active at $\eta = 65$ mV, exhibiting an exceptional current density of ~330 mA cm^{-2}, FE of 85%, and TOF of 0.28/s in a 50:50 vol% ionic liquid/water electrolyte for CO production surpassing other known CO_2 reduction electrocatalysts (Fig. 6). The superior properties of the WSe_2 NFs were attributed to their much lower charge-transfer resistance (*R*ct) and significantly low work function (3.52 eV). In addition, DFT calculations revealed that CO was stabilized on TMD edges, indicating the formation of CO from CO_2 was kinetically favorable.

Moreover, alloying and doping different metals with TMD materials may further push their performance to the limit and optimize the binding energies of the reaction intermediates such as *CO [146]. Further, doping can tune the binding strengths of different intermediates and the reaction energetics, thus modifying the activity and selectivity of the CO_2 reduction reaction. For example, Abbasi et al. reported 5% niobium (Nb)-doped vertically aligned MoS_2 in an ionic liquid that exhibited the smallest onset overpotential of 31 mV and one order of magnitude higher CO formation TOF than pristine MoS_2, which was two times higher than that of Ag NPs within an overpotential range of 50–150 mV and 100–650 mV, respectively [147]. The presence of Nb was proposed to facilitate the rapid release of CO from the TMD edge. Similarly, Ta-doped MoS_2 catalysts were also studied as another candidate, but they showed lower performance than the pristine vertically aligned MOS_2 due to a change in the binding energy of Ta and MoS_2, as shown in Fig. 7. However, progress within this family of materials will be achieved upon their further study. Summary of metal and TMD-based catalysts for electrocatalytic CO_2 reduction is provided in Table 3.

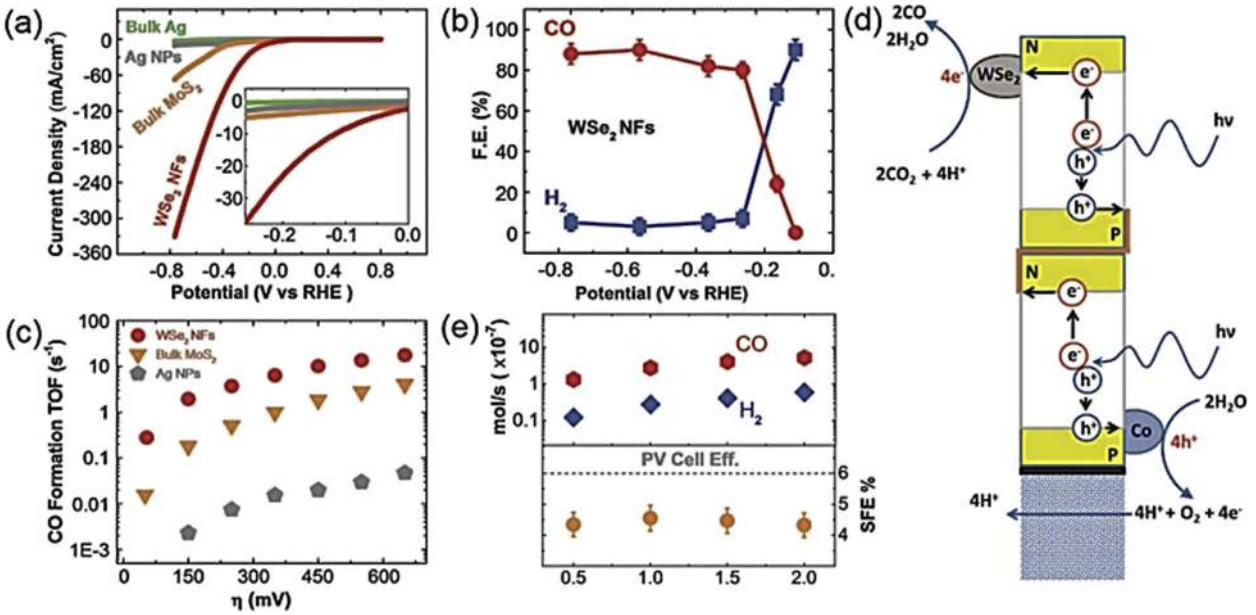

Fig. 6. (a) CV curves recorded for WSe_2 NFs, bulk MoS_2, Ag NPs, and bulk Ag in a CO_2 saturated EMIM-BF_4/H_2O solution, (b) potential-dependent FE for CO and H_2 on WSe_2 NFs, (c) CO formation TOF of WSe_2 NFs, bulk MoS_2, and Ag NPs, and (d) a schematic representation of an artificial leaf with a WSe_2 cocatalyst used to reduce CO_2 to CO under light illumination. (e) Product formation rates under different intensities of illuminated light using the WSe_2/IL cocatalyst system. Reproduced with permission [139]; copyright 2016, American Association for the Advancement of Science.

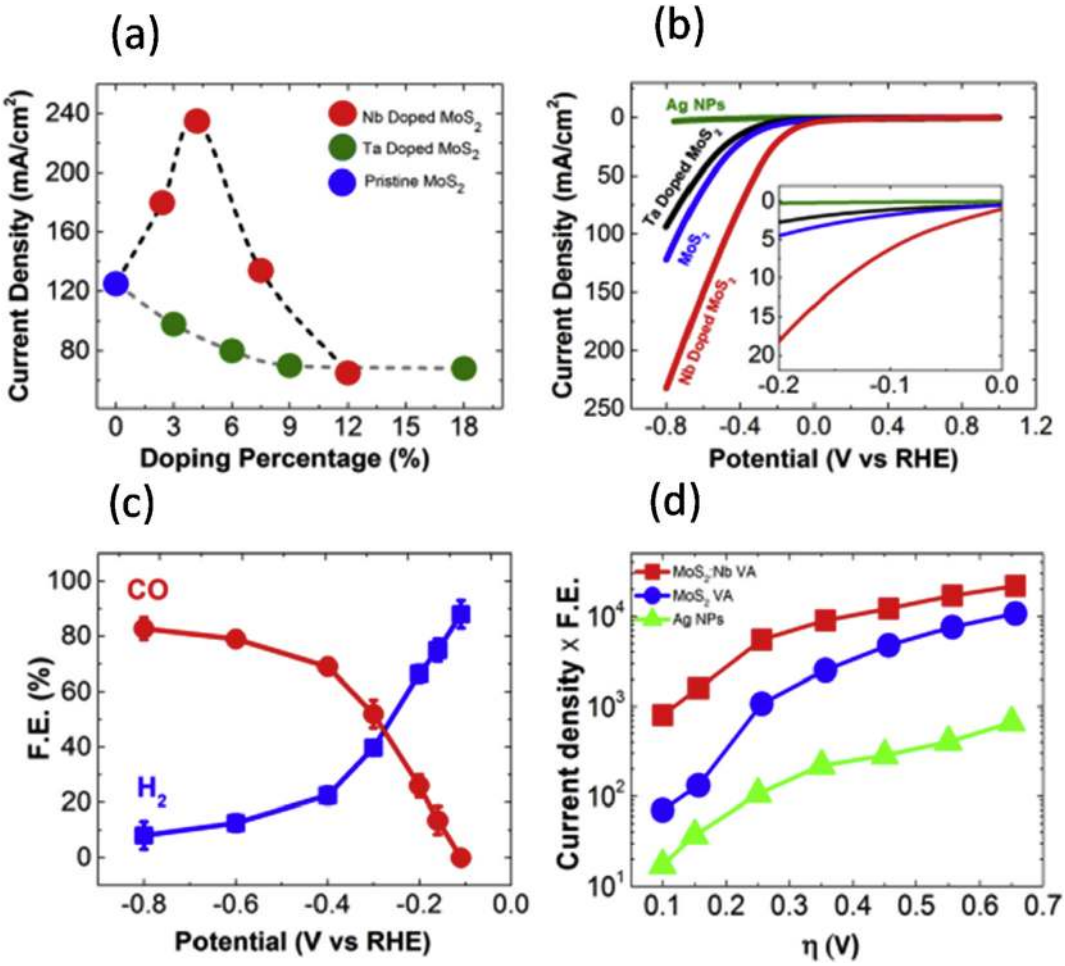

Fig. 7. CO_2 reduction performance of pristine and doped MoS_2 samples. (a) Current density as a function of the dopant percentage for the Nb-doped and Ta-doped MoS_2 samples. (b) CV curves recorded for Ag NPs, VA-MoS_2, VA-$Mo_{0.97}Ta_{0.03}S_2$, and VA-$Mo_{0.95}Nb_{0.05}S_2$ in a CO_2 environment. (c) CO and H_2 FE% observed for VA-$Mo_{0.95}Nb_{0.05}S_2$ at different applied potentials. (d) Partial current density for CO formation observed for Ag nanoparticles, VA-MoS_2, and VA-$Mo_{0.95}Nb_{0.05}S_2$. Reproduced with permission [141]; copyright 2016, American Chemical Society.

3.4. Metal-organic framework based catalysts used in the CO_2 reduction reaction

3.4.1. Preparation and properties of MOFs

MOFs are new porous polymers constructed using metal clusters as secondary building units (SBUs) and organic linkers. Therefore, the geometry of MOFs is determined by these two elements [154]. For example, an octahedral net (i.e., HKUST-1) can be made from tetrahedral SBUs using linear linkers, whereas the combination of octahedral SBUs and linear linkers can be used to create a cubic topology (i.e., MOF-5) (Fig. 8) [155].

The synthesis of MOFs can be implemented using many different methods, as shown in Fig. 9 [156–158]. Factors including the temperature, solvent composition ratio, reactant concentration, and reaction times have been thoroughly investigated to find the optimal conditions to form MOF crystals [159]. For example, Haque and Jhung researched a famous family of MOF materials, M-MOF-74 (M = Zn, Co, and Ni), which were synthesized using three methods: ultrasound, microwave, and conventional heating [160]. This study revealed that the MOF crystals were formed with different sizes as well as porosity. The conventional heating method formed the largest crystal size, while ultrasound generated the smallest MOFs

Table 3
Summary of metal and TMD based catalysts for electrocatalytic CO_2 reduction.

Sample ID	Product	FE (%)	Potential	Ref
3D porous hollow fiber Cu	CO	75	−0.4 V vs. RHE	[148]
Au/carbon nanotubes (CNT)	CO	94	−0.5 V vs. RHE	[149]
Nanoporous Ag	CO	92	−0.6 V vs. RHE	[150]
Au NW	CO	94	−0.35 V vs. RHE	[151]
Cu NPs	CH_4	80	−1.25 vs. SHE	[152]
Bulk MoS_2	CO	98	−0.764 V vs. RHE	[51]
WSe_2	CO	85	−0.764 V vs. RHE	[53]
N-doped graphene quantum dots (QDs)	C_2H_4	46	−0.86 V vs. RHE	[153]
N-doped graphene QDs	C_2H_5OH	21	−0.86 V vs. RHE	[153]
N-doped graphene QDs	CO	23	−0.6 V vs. RHE	[153]

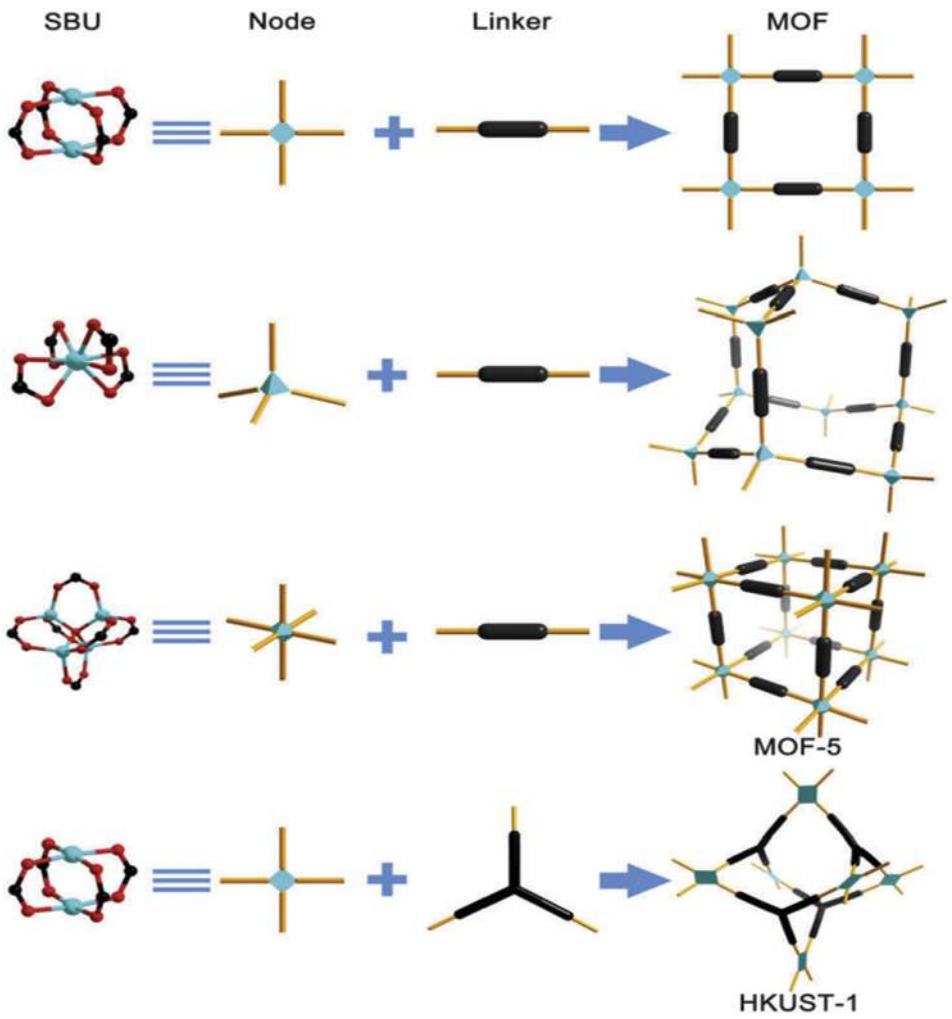

Fig. 8. A graphical illustration of the construction of some MOFs from SBU and rigid linkers. Reproduced with permission [155]; Copyright 2014 Chemical Society Reviews.

in the shortest time. Moreover, an electrochemical method was reported for the synthesis of MOF (HKUST-1) for the first time in 2005 [161]. The author used copper plates (thickness, 5 mm) for the anode in the electrochemical system, 1,3,5-benzenetricarboxylic acid dissolved in methanol as the electrolyte, and a copper cathode. A blue crystal was generated after 150 min of electrolysis at 12–19 V. Recently, green synthetic methods have been studied to develop sustainable and eco-friendly processes. MOFs can be synthesized in the solid phase or in an aqueous media [162].

MOFs are the quintessential products of the combination of inorganic and organic chemistry. They are the most beautiful compounds ever made and have become famous materials with wonderful abilities in a wide range of applications including gas adsorption, separation, catalysis, drug storage, sensors, and batteries due to their large specific area, high pore volume, and structural diversity [163]. As a case in point, Mg-MOF-74 is known to display the highest CO_2 adsorption capacity, which plays a vital role in its catalytic activity toward the CO_2 reduction reaction [164]. Therefore, several studies have discussed the yield of the CO_2 reduction reaction on a Mg-MOF-74 based photocatalyst. According to a study carried out in 2005, nine isostructural Mg-MOF-74 derivatives were generated upon adding phenyl groups into the initial ligand to change the pore size of the MOF material [73]. The results showed that the range of pore aperture was 14–98 Å. Moreover, by using advanced computational tools many research teams have provided huge databases of theoretical MOFs, which can be experimentally prepared. For instance, Wilmer et al. generated more than 137,000 hypothetical MOFs using various inorganic building blocks and ligands [165]. This is very useful for the discovery of an ideal material for the specific applications based on the estimated properties. In addition, the unsaturated metal sites in MOFs are crucial for catalytic applications such as the HER and CO_2 reduction reaction [166].

3.4.2. MOF-based electrocatalysts used in the CO_2 reduction reaction

MOFs have been scrutinized in the field of catalysis, such as the HER, oxygen evolution reaction (OER), and CO_2 reduction reaction [167–170]. Due to their unique abilities, MOF-based catalysts can display high product selectivity in the CO_2 conversion process. Catalysts including pristine MOFs and MOFs-hybrid for electroreduction CO_2 were shown in Table 4.

For example, Kornienko et al. created a thin film consisting of a cobalt-porphyrin MOF on a carbon substrate in 2015 (Fig. 10a and b) [168]. Two main products (CO and H_2) were detected using gas chromatography and nuclear magnetic resonance spectroscopy. As presented in Fig. 10c, the FE of this material was 76% at −0.7 V vs. RHE in the transformation of CO_2 into CO. Moreover, a low Tafel slope of 165 mV/decade was also observed (Fig. 10d) and the catalytic stability was also tested over 7 h with a turnover number of

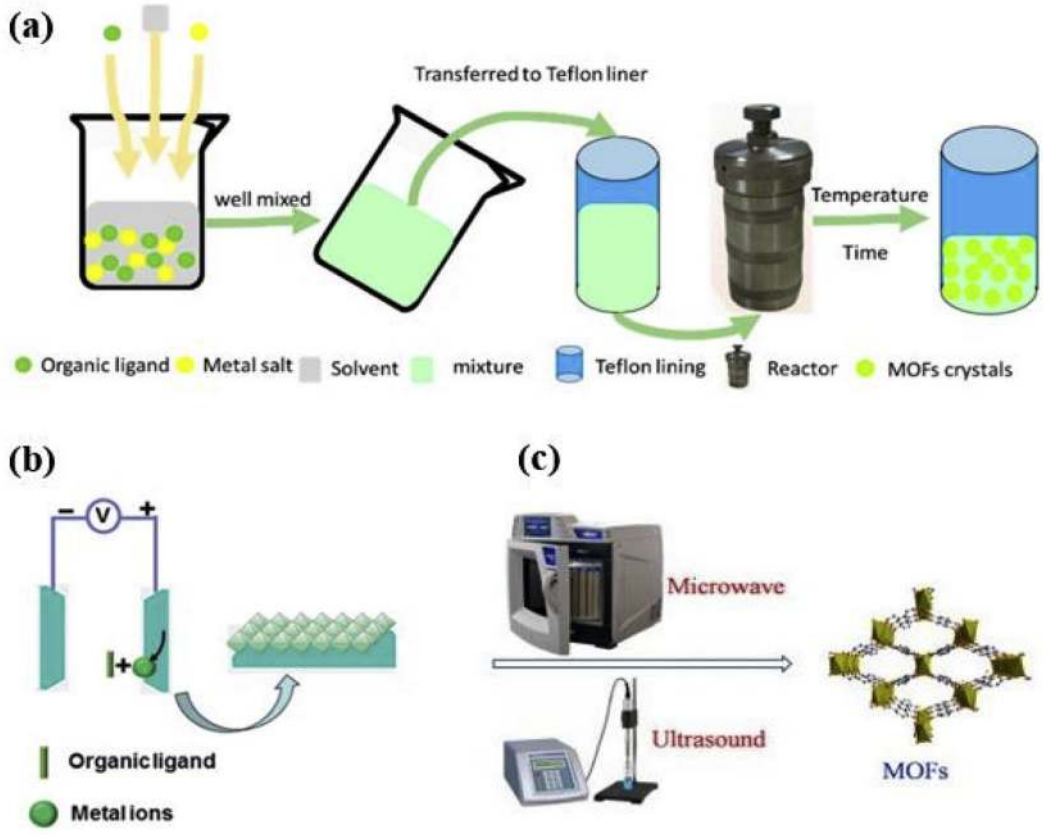

Fig. 9. Schematic representations of different MOF synthesis techniques: (a) solvent heating method (reproduced with permission from [156]; Copyright 2018, Processes), (b) electrochemical method (reproduced with permission from [161]; Copyright 2016, The Royal Society of Chemistry), (c) microwave and ultrasound method (reproduced with permission [158]; Copyright 2015 Coordination Chemistry Reviews).

1,400. Wang et al. synthesized ZIF-8 from different sources of Zn, including $ZnSO_4$, $Zn(OAc)_2$, and $Zn(NO_3)_2$ for CO_2 electroreduction [172]. This sample was coated onto the surface of glassy carbon electrodes to create the working electrode in the electrocatalytic CO_2 reduction process. The electrochemical reaction was implemented in the various electrolytes, involving 0.5 M $NaHCO_3$, NaCl and $NaClO_4$. The result indicated that ZIF-8, formed from $ZnSO_4$ exhibited outstanding performance with a Faradaic yield of 65.5% for CO at −1.8 V vs. SCE. The improved activity was attributed to Zn metal sites in the ZIF-8 structure. Besides, electrolytes have an effect on the selectivity of electrochemical reaction. The FE of CO in $NaHCO_3$ is the lowest at specific potential compared with NaCl and $NaClO_4$, while NaCl gave the highest performance.

Many studies have indicated that copper metal has the distinct property to generate a series of products such as carbon monoxide, methane, ethylene, methanol, and ethanol [179]. To remediate this issue, the combination of copper and MOF materials can produce promising candidates for the CO_2 reduction reaction with high selectivity. Thus, Hinogami et al. examined the electrocatalytic ability of copper rubeanate metal-organic frameworks (CR-MOFs) [167]. A working electrode was fabricated by coating CR-MOF onto carbon paper with a thickness of 0.36 mm. The catalytic performance was studied in a 0.5 M $KHCO_3$ solution using platinum wire as the counter electrode and AgCl/Ag as the reference electrode. The results demonstrated that formic acid was the main reductant in the conversion of CO_2 with 98% selectivity. When compared to

Table 4
Summary of MOF-based catalysts for electrocatalytic CO_2 reduction.

Sample ID	Product	FE (%)	Potential	Year	Ref
Zn-BTC	CH_4	80.1 ± 6.6	−2.2 V vs. Ag/AgCl	2016	[171]
ZIF-8	CO	65.5	−1.8 V vs. SCE	2017	[172]
Re-SURMOF	CO	93 ± 5	−1.6 V vs. NHE	2016	[173]
M-PMOF	CO	98.7	−0.8 V vs. RHE	2018	[174]
CR-MOF	HCOOH	98	−1.2 vs. SHE	2012	[167]
$Al_2(OH)_2$TCPP-Co	CO	76	−0.7 V vs. RHE	2018	[168]
ZIF-CNT-FA-p	CO	100	−0.86 V vs. RHE	2017	[175]
Ru(III)-doped HKUST1	CH_3OH, C_2H_5OH	47.2	20 mA cm^{-2}	2018	[170]
Ag_2O/layer ZIF	CO	80.5	−1.2 V vs. RHE	2017	[176]
ZIF-8 derived Fe−N−C	CO	91	−0.6 V vs. RHE	2017	[177]
C-AFC@ZIF-8	CO	93	−0.6 V vs. RHE	2017	[178]

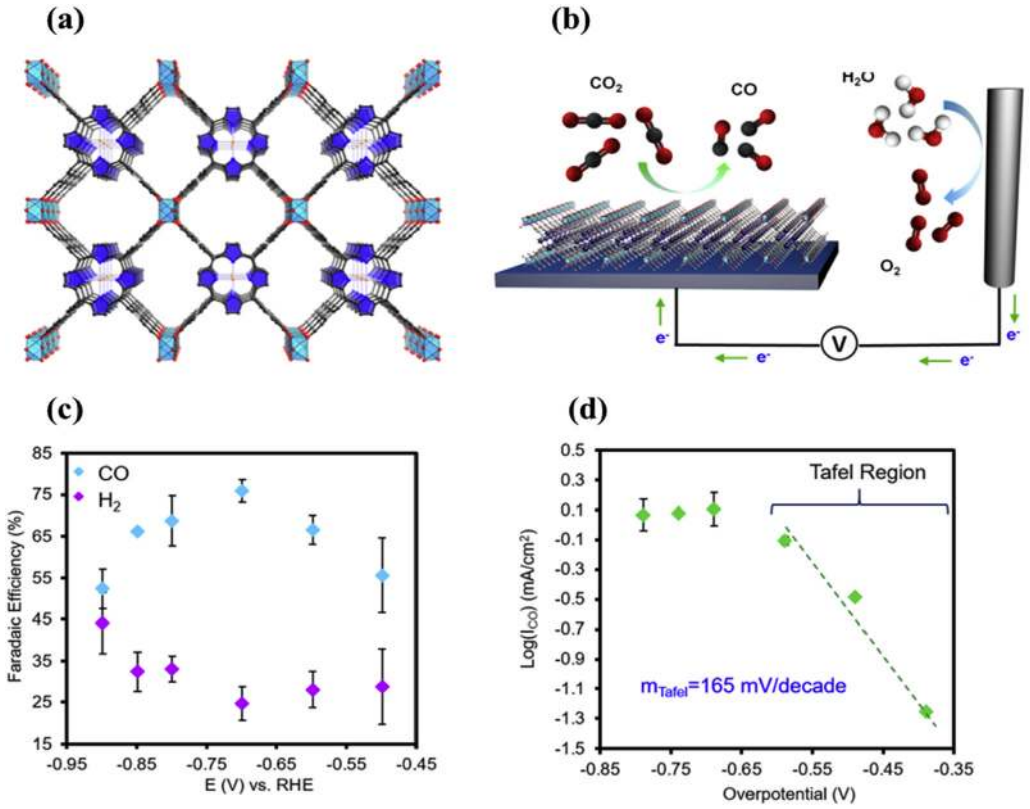

Fig. 10. (a) The structure of a $Al_2(OH)_2TCPP$-Co MOF (the spheres in black, red, orange, and blue denote C, O, Co, and N, respectively; the light-blue octahedral and blue ring represent Al and pyrrole, respectively). (b) The MOF is coated on a carbon substrate for the electroreduction reaction (c) The selectivity of the reductants was checked over a potential range of −0.5 to −0.9 vs RHE (V). (d) Tafel slope of the MOF material. Reproduced with permission [168]; Copyright 2018, Wiley-VCH.

the copper electrode, the HCOOH formation rate was 13.4 μmol cm^{-2}/h on the CR-MOF, while that on the Cu electrode was 1.1 μmol/cm^2/h at −1.2 V vs. SHE. The enhanced selectivity was attributed to the weaker CO_2 adsorption of CR-MOF caused by the reduced electron density on the metal sites.

Although MOFs have unique structural characteristics, the poor conductivity limited their electrocatalytic applications. Thus, MOFs have become ideal precursors to fabricate MOF-hybrid porous materials such as metal nanoparticle doped carbon, and metal-free nanocarbon. Very recently, a study on Cu-based MOF was published by Perfecto-Irigaray et al. [170]. The author doped a few metals (Zn, Pd and Ru) into HKUST-1 at different ratios to assess their electrocatalytic activity in the CO_2 reduction reaction. The results revealed that Ru-doped HKUST-1 exhibited a FE of 47.2% with an optimal Ru(III) amount of 10%. The other metals did not give good results when compared to the bare HKUST-1. However, in all cases, doping metals into the MOF enhanced the selectivity toward ethanol, which could reach 100%. This was attributed to the formation of a C—C bond on the metal sites that created C_2—C_3 products, which were then released to form alcohol or ketone products.

4. Materials used as efficient photocatalysts in the CO_2 reduction reaction

Photocatalytic reduction of CO_2 motivated by natural photosynthesis in green plants is one of the most promising and captivating approaches. Several types of catalysts have been reported in the field of CO_2 photoreduction, including metal oxides [180,181], metal sulfides [182,183], graphitic carbon nitride, GO, carbon nanofiber [184,185], carbon quantum dots [186], and metal—organic frameworks [187].

4.1. Metal oxides

Metal oxides are a very common type of photocatalyst used in the CO_2 reduction reaction. A large number of them consist of transition metal cations (e.g., Ti^{4+}, Zr^{4+}, Nb^{5+}, Ta^{5+}, W^{6+}, and Mo^{6+}) with the d^0 configuration. Due to its excellent stability, non-toxicity, low cost, and ease of availability, TiO_2 is one of the most widely studied photocatalysts, while TiO_2-based 2D nanosheets prepared via the exfoliation of layered titanate have also drawn considerable research interest [188]. Xu et al. synthesized anatase TiO_2 single crystals composed of ultrathin TiO_2 nanosheets (thickness, 2 nm) with 95% of exposed (100) facets, which exhibit ~5 times higher activity in both the HER and CO_2 reduction reaction when compared to TiO_2 cuboids with 53% of exposed (100) facets. For the TiO_2 nanosheets, on one hand, the higher percentage of exposed (100) facets and larger surface area can offer more surface active sites. On the other hand, the superior electronic band structure, which results from the higher percentage of the exposed (100) facets contributes to their expanded activity.

Moreover, ultrathin, single-crystal WO_3 nanosheets with a thickness of 4—5 nm, which corresponds to six repeating unit cells of monoclinic WO_3 along the *c*-axis, have been synthesized via the lateral oriented attachment of tiny WO_3 nanocrystals formed via a solid—liquid phase arc discharge process [189]. Because of size-quantization effects in this ultrathin nanostructure that extend

the WO_3 band gap,WO_3 nanosheets exhibit enhanced performance for the photocatalytic reduction of CO_2, which does not occur in the bulk form (Fig. 11).

4.2. Transition metal di-chalcogenides

When compared to their oxide counterparts, metal sulfides possess higher valence bands mainly with S3p character and narrower band gaps. It is, however, a general concern that the photogenerated holes on their valence band may not be energetic enough to oxidize water and will instead result in their irreversible photocorrosion. As a result, hole scavengers are frequently added in order to extend their stability. CdS is a well-known visible light photocatalyst, which has a band gap (2.4 eV) that matches well with the solar spectrum [190]. In 1988, Eggins et al. reported for the first time the photocatalytic performance of CdS in the CO_2 reduction reaction under visible light irradiation, yielding formaldehyde, methanol, formate, acetate, and glyoxylate as the main products [191]. In other studies, Tu et al. fabricated 2D MoS_2 nanosheets grown in situ on TiO_2 nanosheets to form a 2D hybrid nanojunctions, in which the MoS_2 nanosheets were in contact with TiO_2 to increase the interfacial area [192]. The MoS_2—TiO_2 hybrid nanojunction exhibited superior activity and selectivity in the reduction of CO_2 to form CH_3OH in an aqueous solution under UV—Vis light irradiation. Different MoS_2 contents, such as 0.5, 1, 2, and 3 wt%, were investigated. Thus, the CH_3OH production rate of 0.5 wt% MoS_2/TiO_2 (10.6 μmol/g/h) was ~2.9 times higher than that of pure TiO_2 (3.7 μmol/g/h), which indicated that MoS_2 served as an efficient cocatalyst. However, further increasing the MoS_2 content (from 1 to 3 wt%) leads to a gradual decrease in the photocatalytic activity due to the shielding effect of MoS_2 on the TiO_2 surface. Moreover, Ali and co-workers reported WSe_2—graphene nanocomposites prepared via ultrasonication and investigated them in terms of the photocatalytic reduction of CO_2 to form CH_3OH under irradiation with UV/visible light [193]. Adding a sacrificial agent (Na_2S/Na_2SO_3) to the WSe_2—graphene nanocomposites further improved the photocatalytic efficiency. After coupling with graphene, the resulting binary structure promoted electron transport and reduced the recombination of the electron—hole pairs when compared to pure WSe_2. This was the first article reporting that the WSe_2 chalcogenide family could be used as a photocatalyst in the CO_2 reduction reaction.

4.3. MOF-based photocatalysts used in the CO_2 reduction reaction

In 2011, Wang et al. reported the first MOF-based heterogeneous catalyst used in the CO_2 reduction reaction [194]. MOF **4** was prepared using a combination of $ZrCl_4$, dicarboxylic acid, and $Re(CO)_3(dcbpy)Cl$ (H_2L_4). The study revealed that MOF **4** displayed the best catalytic activity in the selective reduction of CO_2 to form CO under visible light irradiation using trimethylamine (TEA) as an electron donor. The yield of MOF **4** was 2.8 times higher than H_2L_4. However, the stability of the catalyst was not high. Overall, the pure MOF shows low productivity for CO_2 photoreduction [195]. MOFs can be modified using many different strategies to enhance their catalytic activity. These results were provided in Table 5 [78,194,196—210]. A popular way is to generate a TiO_2/MOF composite. Li et al. created a $Cu_3(BTC)_2$@TiO_2 nanocomposite via a hydrothermal method [199]. The amount of TiO_2 in the composite was 33 wt%. Photocatalytic tests were implemented using a 300 W xenon arc lamp as the light source for the reaction. Although the addition of TiO_2 on HKUST-1 reduced the CO_2 adsorption ability, the CH_4 production rate was significantly increased from 0.52 (TiO_2) to 2.64 μmol/g/h. A CPO-27-Mg/TiO_2 nanocomposite was investigated by Wang et al. [195]. This material displayed photocatalytic activity under UV irradiation at 365 nm in the presence of water vapor. CPO-27-Mg/TiO_2 produced CH_4 and CO at a faster rate than CPO-27-Mg, which did not exhibit any photocatalytic activity in the CO_2 reduction reaction. In comparison to TiO_2, CPO-27-Mg/TiO_2 shows nearly two times higher activity. This was attributed to the improved CO_2 adsorption capacity of the nanocomposite. The MOF hybrid catalysts led to a shift in the electronic properties as well as the adsorption characteristics of the MOF, which enhanced their catalytic activity. As another example for this case, Liu et al. combined ZIF-8 NPs with Zn_2GeO_4 nanorods in order to boost their photocatalytic performance in the CO_2 reduction reaction [197]. The reaction system was conducted under visible light irradiation. In the presence of Na_2SO_3, CO_2 was photoreduced into CH_3OH at a rate of 0.22 μmol/g/h using the Zn_2GeO_4/ZIF-8 nanorods. When compared to the homogenous system, Zn_2GeO_4 has a conversion speed of 0.143 μmol/g, whilst the ZIF-8 particles did not create any product during the CO_2 reduction reaction.

An alternative strategy to boost the catalytic ability of MOFs is to modify the MOF linkers using amino groups. A number of experimental reports have demonstrated that the CO_2 adsorption capacity, optical absorption characteristics, and CO_2 photoreduction yield of MOFs can be remarkably enhanced upon the addition of NH_2 [78,200,211]. Fu et al. synthesized a NH_2-MIL-125(Ti) photocatalyst for CO_2 reduction by changing the BDC linker in MIL-125(Ti) with a NH_2-BDC linker [78]. Photocatalytic experiments were carried out under visible light irradiation in MeCN/TEOA. Formate ions were detected with a yield of 16.3 μmol/g/h, while the unmodified MOF was inactive. The study results revealed that the photocatalytic activity of NH_2-MIL-125(Ti) can be improved by

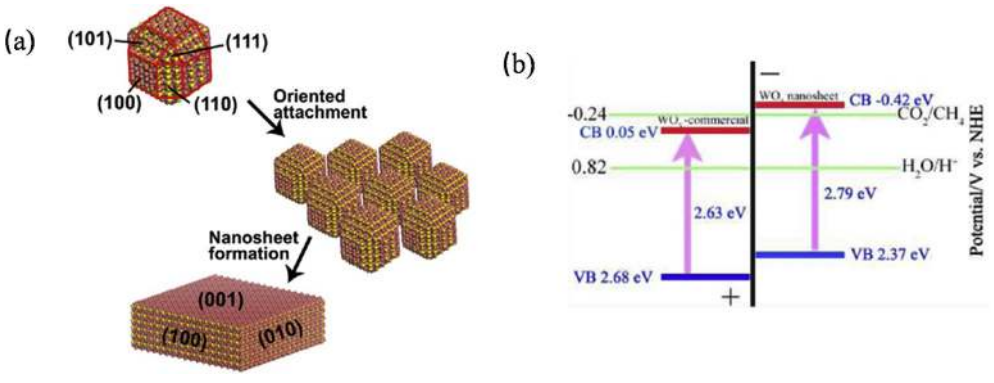

Fig. 11. (a) A schematic illustration of WO_3 nanosheet formation from small nanocrystals, (b) band position of the WO_3 nanosheet and commercial WO_3 relative to the redox potential of CO_2/CH_4 in the presence of water. Reproduced with permission [169]; Copyright 2012, American Chemical Society.

Table 5
Summary of MOF-based catalysts for photocatalytic CO_2 reduction.

Sample ID	Proton donor	Product and yield (μmol/g h)				Light source	Year	Ref
MOF **4**	TEA	CO 10.9				UV	2011	[194]
NH_2-MIL-125(Ti)	TEOA	$HCOO^-$ 16.3				Visible	2012	[78]
Copper porphyrin MOF[a]	TEOA	CH_3OH[b] 262.6				Visible	2013	[196]
Zn_2GeO_4/ZIF-8	H_2O	CH_3OH 0.22				UV	2013	[197]
Pt−NH_2-MIL-125(Ti) Au−NH_2-MIL-125(Ti)	TEOA	$HCOO^-$ 32.4 16.3					2014	[198]
$Cu_3(BTC)_2$@TiO_2	H_2O	CH_4[c] 2.64				UV	2014	[199]
NH_2-UiO-66(Zr) NH_2-UiO-66(Zr/Ti)	TEOA	$HCOO^-$[d] 3.4 5.8				Visible	2015	[200]
Ui-66-CrCAT Ui-66-GaCAT	TEOA	HCOOH 1724 959					2015	[201]
Co-ZIF-9 Co-MOF-74 Mn-MOF-74 Zn-ZIF-8	TEOA	CO 12.6 9.9 0.3 0.2	H_2 2.8 1.9 0.5 0.2		TON	Visible	2015	[202]
CPO-27-Mg/TiO_2 TiO_2 CPO-27-Mg	H_2O	CO 4.09 2.25 0		CH_4 2.35 1.37 0		UV	2015	[195]
Co-ZIF-9/TiO_2	H_2O	CO 8.8		H_2 2.6		UV−Vis	2016	[204]
PCN-22	TEOA	$HCOO^-$ 52.8				Visible	2016	[203]
Zn/PMOF	H_2O	CH_4 8.7				UV−Vis	2016	[205]
2Cu/ZIF-8N2	Na_2SO_3	CH_3OH[e] 35.82				Visible	2018	[206]
Ag@Co-ZIF-9	TEOA	CO[f] 28.4		H_2 22.9		Visible	2018	[207]
Ni MOLs	TEOA	CO 12.5		H_2 0.28		Visible	2018	[214]
TiO_2/Cu_2O/$Cu_3(BTC)_2$	H_2O	CO 210		CH_4 160		Visible	2018	[209]
Zn-MOF nanosheets/ $[Co_2(OH)L](ClO_4)_3$	TEOA	CO 14.45		H_2 2.6		Visible	2018	[213]
NH2-rGO (5 wt%)/Al-PMOF	TEOA	$HCOO^-$ 685.6				Visible	2018	[212]
CdS/UiO-bpy/Co	TEOA	CO 235				Visible	2018	[209]
ZIF-67_1 ZIF-67_2 ZIF-67_3	TEOA	CO 3.75 3.06 3.89				Visible	2018	[210]

[a] (5,10,15,20-tetrakis(4-carboxyphenyl) porphyrin.
[b] Production in ppm/g_{cat} after 1 h operation.
[c] Average after 4 h operation.
[d] Production in mmol/mol_{cat} after 10 h operation.
[e] Production in μmol/L.g after 6 h operation.
[f] Production in μmol after 0.5 h operation.

increasing the CO_2 adsorption capacity and expanding their optical absorption. Besides, the reduction Ti^{4+} to Ti^{3+} due to electron transfer from the amine-functionalized linker creates convenient conditions for CO_2 conversion to form $HCOO^-$.

At present, the highest rate for converting CO_2 to HCOOH was reported by Lee et al. [201]. The author attached Cr and Ga onto the linker of UiO-66 via a catechol group to generate UiO-66-CrCAT and UiO-66-GaCAT. The photoreaction was performed under visible light irradiation in a solution containing MeCN/TEOA. UiO-66-(M) CAT (M = Cr and Ga) shows good catalytic activity and the bare MOF was inactive. Obviously, HCOOH was formed during the photocatalytic reaction with a yield of 20 ,692 μmol/g/h observed for UiO-66-CrCAT and 11 ,512 μmol/g/h for UiO-66-GaCAT.

As mentioned above, graphene has unique electronic properties. Thus, the incorporation of graphene and MOF materials is considered as a perfect couple for catalytic applications. As a result, Sadeghi et al. reported the first graphene-based MOF heterogeneous catalytic system for the photocatalytic CO_2 reduction reaction [212]. Tetrakis(4-carboxyphenyl) porphyrin (TCPP) was used as an organic linker to synthesize a variety of Al-PMOF materials. GO was reduced and modified using amino groups to prepare NH_2-rGO. Thereafter, the NH_2-rGO/Al-PMOF composites were generated

using different ratios to investigate their catalytic ability for CO_2 conversion. Photocatalytic reactions were carried out under visible light irradiation with TEOA used as an electron donor. The results indicated that NH_2-rGO (5%)/Al-PMOF showed the best result for CO_2 reduction with a formate production rate of 685.6 μmol/g/h when compared to the other composites. The reason for this is that a negative effect on the optical adsorption ability is observed with MOF composites containing >5% NH_2-rGO, which leads to a decrease in the electron–hole pair production rate. Moreover, the performance of NH_2-rGO (5%)/Al-PMOF was also better than bare MOF and TCPP. Formate ions were formed on NH_2-rGO (5%)/Al-PMOF with a yield of 205.6 μmol over 6 h, while this value is 49.6 μmol for Al-PMOF and 4.56 μmol for TCPP under the same reaction conditions. The enhanced activity was attributed to the higher surface area created by graphene. This leads to an increase in the number of active sites, which contribute to the catalytic activity of material. The mechanism for the reaction suggests that TCPP plays an important role in the CO_2 reduction process. Under visible light irradiation, the electron–hole pairs are separated on the organic linker (TCPP) and the electrons move to graphene and the holes stay on the TCPP linker. These electrons are accepted by the CO_2 molecules absorbed on the catalytic material during the conversion of CO_2 into $HCOO^-$.

Recently, two-dimensional metal-organic framework (2D MOF)-based nanosheets have received an increasing amount of attention due to their outstanding characteristics such as ultrathin thickness, high surface area, and adjustable structure. 2D MOFs are a new topic in 2D materials and they contain many highly active centers on their surface, which are useful for catalytic applications. The first 2D MOF used for CO_2 photoreduction was reported by Ye et al. in 2018 [213]. Zn-TCPP nanosheets were prepared using a surfactant-assisted method, while bulk Zn-TCPP material was prepared by traditional synthesis. The photocatalytic performance was investigated under irradiation with a Xe lamp in MeCN/MeOH/TEOA. The 2D MOF was incorporated with a metal complex ($[Co_2(OH)L](ClO_4)_3$) or ZIF-67, and acts as a co-catalyst (Fig. 12a). In both cases, the catalytic activity of the Zn-TCPP nanosheets was enhanced when compared to their bulk materials (Fig. 12b and c). This was attributed to the higher absorption ability of CO_2 on the Zn-TCPP nanosheets when compared to the bulk Zn-TCPP material. Besides, creating the 2D MOF hybrid increased the efficiency of electron transfer and lifetime, which enhanced the catalytic performance of the 2D MOF nanosheets.

Another 2D MOF nanosheet material is Ni MOLs, synthesized by Han et al., in 2018 [214]. Ni MOLs monolayers were generated using a top-down strategy with the combination of an ultrasonic system and an enormous amount of water to avoid restacking of the MOF nanosheets (Fig. 13a). The thickness of the Ni MOLs was ~1.0 nm, which was confirmed by AFM. The catalytic activity was carried out under visible light irradiation under different conditions using $[Ru(bpy)_3]Cl_2 \cdot 6H_2O$ as a photosensitizer. In the presence of TEOA, CO_2 was photoreduced to CO and H_2. Single-layered Ni MOFs showed the best results in pure CO_2 with a CO generation rate of 12.5 μmol/h and H_2 formation rate of 0.28 μmol/h. In terms of diluted CO_2 (10%), the apparent quantum efficiency of the Ni MOFs nanosheets was 1.96% with a CO selectivity of 96.8%, which is the

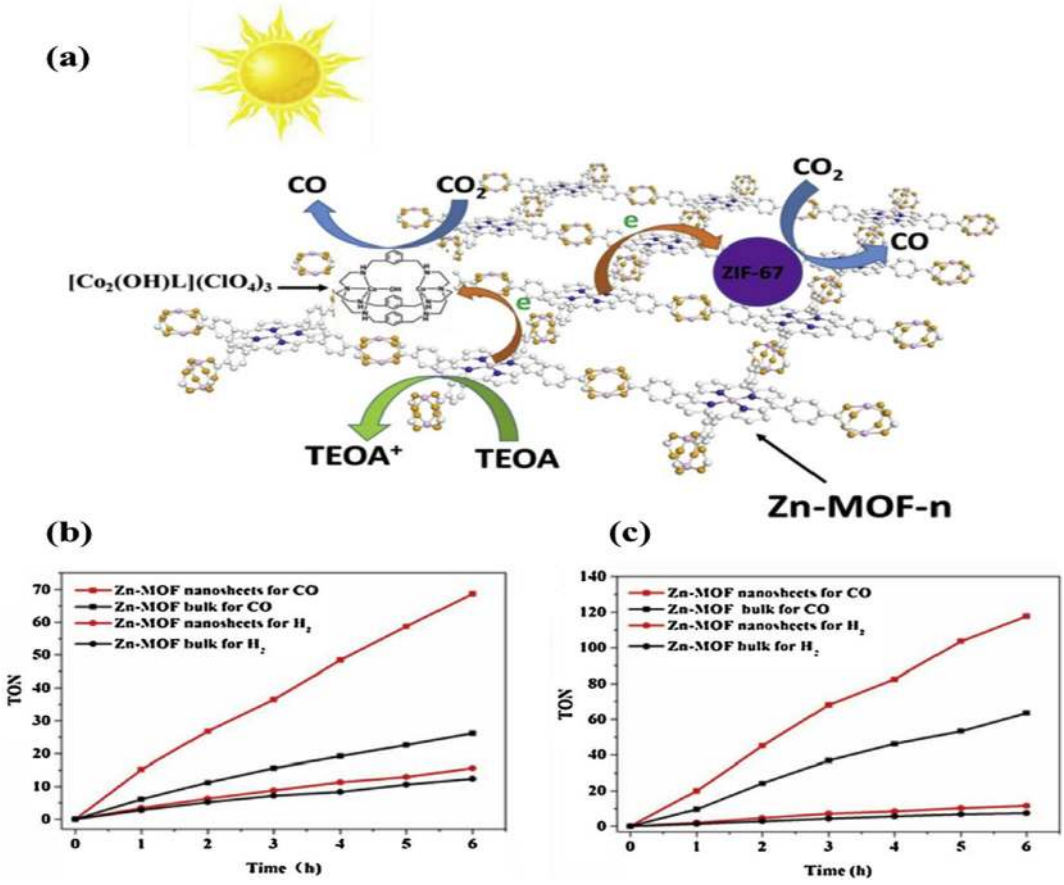

Fig. 12. Evolution of the CO_2 photoreduction products under Xe lamp irradiation for 6 h using: (a) A MOF/complex or MOF/ZIF system for the photocatalytic reduction of CO_2 with Zn-MOF nanosheets as a photosensitizer, (b) Zn-MOF nanosheets or Zn-MOF bulk as a photosensitizer and $[Co_2(OH)L](ClO_4)_3$ as the cocatalyst, and (c) Zn-MOF nanosheets or Zn-MOF bulk used as a photosensitizer and ZIF-67 as the co-catalyst. Reproduced with permission [213]; Copyright 2018, Applied Catalysis B.

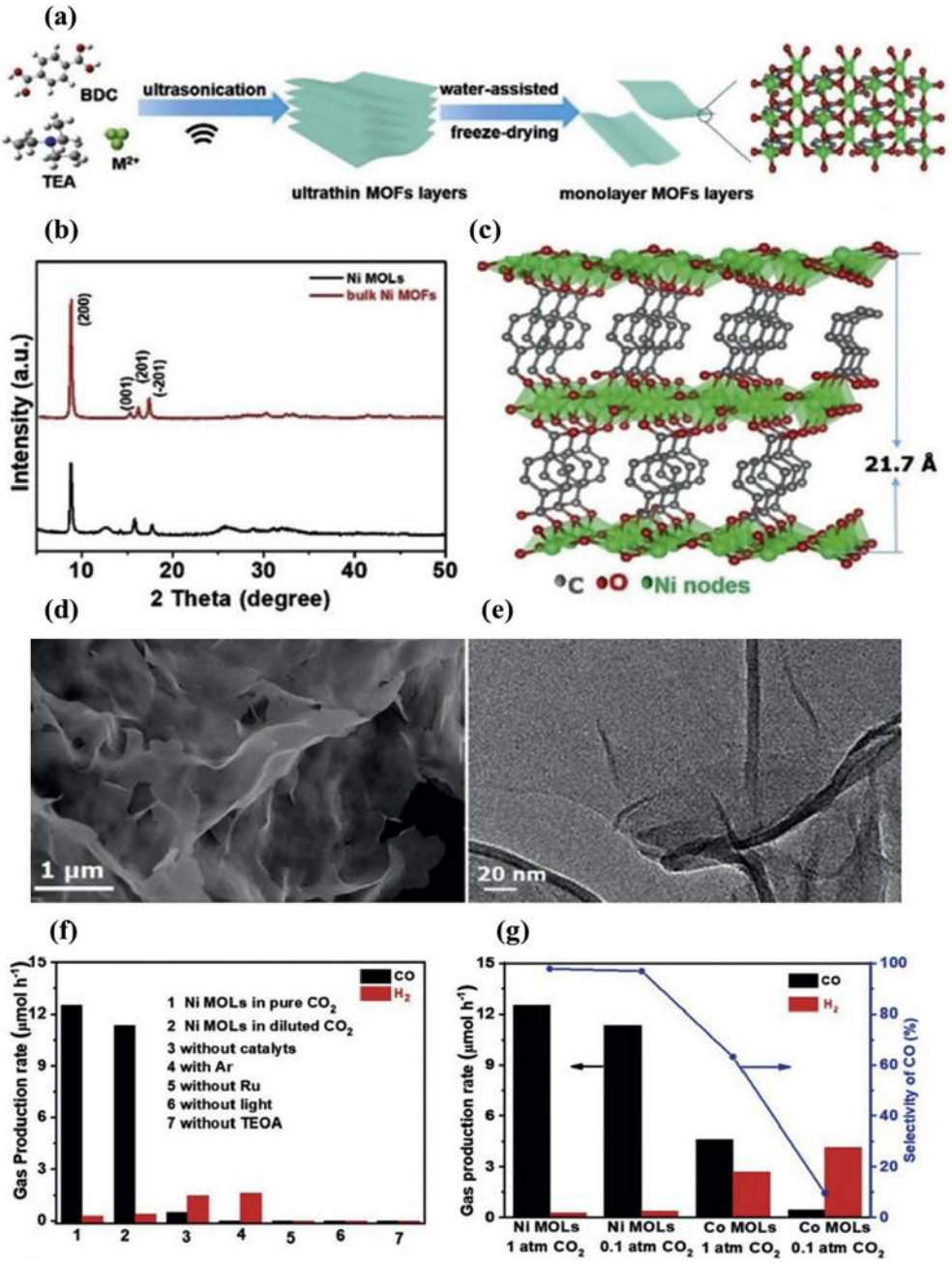

Fig. 13. (a) A schematic illustration of the generation of Ni MOLs, (b) XRD pattern, (c) atomic arrangement, (d) SEM image, (e) TEM image of Ni MOLs, (f) CO_2 photoreduction performance under various reaction conditions, and (g) CO_2 photoreduction performance over Ni MOLs and Co MOLs in pure and diluted (10%) CO_2. Reproduced with permission [214]; Copyright 2018, Wiley-VCH.

best value reported to date for this application (Fig. 13b). However, Co MOFs monolayers showed no activity in diluted CO_2 (Fig. 13c). Moreover, these results indicate that CO_2 absorption plays a vital role in the CO_2 reduction process.

5. Conclusions

In this review, the application of 2D materials and MOFs for CO_2 conversion has been discussed from the aspect of electrocatalysis and photocatalysis. Recently emerging 2D materials have made profound progress in the electrocatalytic and photocatalytic reduction of CO_2, yet there are still some challenges in their practical application. Many of the discussed catalysts show high current density and selectivity for simple C_1 products at low overpotential. In fact, research on catalysts used for the electrocatalytic and photocatalytic reduction of CO_2 is at an early stage and needs further study to understand the process mechanism in order to create new more efficient catalysts.

In another case, the birth of MOFs has made the life of researchers become more interesting due to their exclusive properties. They have become promising materials in the field of catalysis. The chemical composition of MOFs plays a crucial role in changing their electronic properties as well as catalytic activity. A large number of research studies on MOF-based photocatalysts used for CO_2 conversion have been reported in order to find the most effective catalytic materials that can be used on an industrial scale. An ideal catalyst should have a

reasonable HUMO−LUMO gap width to absorb solar energy, and the LUMO energy level of the organic ligands should be higher than the redox potential energy level of the metal-oxo centers in order to facilitate the electron transfer process between the ligand and metal centers. Although MOFs show good results in the reduction of CO_2, a big challenge for scientists is the stability of MOF materials in aqueous media. Water usually is used as a special guest molecule in the photocatalytic reduction of CO_2. It provides proton in the CO_2 reduction reaction, but it can cause the collapse of the framework structure by creating a bond with the metal sites and replacing the linker molecules, leading to a reduction in their catalytic activity. The pyrolysis of MOFs has been studied under an inert atmosphere in order to conserve the key characteristics of MOF materials as well as enhance their stability in the oxygen reduction reaction [215]. Pyrolyzed MOFs also provide powerful frameworks, used as templates to dope heteroatoms to increase the catalytic activity in the water splitting reaction [216]. Thus, this technique can be considered as an innovative solution for generating efficient catalysts for use in the CO_2 reduction reaction.

However, only a few papers on MOF-based catalysts have focused on the electroreduction of CO_2, but the impressive results reported to date have emphasized the use of MOFs as alternative catalysts in this area of research. Nevertheless, high selectivity is a strict requirement for MOF materials. For electrocatalytic systems, the MOFs need to be coated onto conductive substrates to create the working electrode. This affects the electron transfer in the CO_2 reduction process and leads to decreased yields in the catalytic reaction. Besides, recycling MOF materials in both photocatalytic and electrocatalytic applications is still a significant problem and needs to be thoroughly researched to save the cost of manufacturing these catalyst materials on a large scale. Although MOFs contain catalytic sites such as OMSs, functional groups, MOFs have poor conductivity, while graphene is a typical 2D material having high conductivity. Therefore, this combination can improve catalytic activity thanks to the increasing conductivity.

Conflict of interest

The authors declare that they have no known competing financial interests or personal relationships that could have appeared to influence the work reported in this paper.

Acknowledgments

This research was supported by the Bio & Medical Technology Development Program [grant number 2018M3A9H1023141]; the Creative Materials Discovery Program through the NRF funded by Ministry of Science and ICT [grant number 2017M3D1A1039379]; and the Basic Research Laboratory of the NRF funded by the Korean government [grant number 2018R1A4A1022647].

References

[1] J.-R. Li, et al., Coord. Chem. Rev. 255 (15−16) (2011) 1791.
[2] S. Xiang, et al., Nat. Commun. 3 (2012) 954.
[3] A.S. Bhown, B.C. Freeman, Environ. Sci. Technol. 45 (20) (2011) 8624.
[4] T.C. Drage, et al., J. Mater. Chem. 22 (7) (2012) 2815.
[5] Y. Lin, et al., Adv. Energy Mater. 7 (4) (2017) 1601296.
[6] A.S. Agarwal, et al., ChemSusChem 4 (9) (2011) 1301.
[7] E.J. Maginn, What to Do with CO2, ACS Publications, 2010.
[8] Y. Tan, et al., Energy Convers. Manag. 118 (2016) 204.
[9] M. Halmann, Nature 275 (5676) (1978) 115.
[10] T. Inoue, et al., Nature 277 (5698) (1979) 637.
[11] W. Wang, et al., Chem. Soc. Rev. 40 (7) (2011) 3703.
[12] J.W. Maina, et al., Mater. Horiz. 4 (3) (2017) 345.
[13] A. Kumar, Q. Xu, Chem. Nano Mat. 4 (1) (2018) 28.
[14] C. Huang, et al., Energy Environ. Sci. 5 (10) (2012) 8848.
[15] D. Kong, et al., Energy Environ. Sci. 6 (12) (2013) 3553.
[16] X. Chia, et al., ACS Nano 9 (5) (2015) 5164.
[17] M. Chhowalla, et al., Nat. Chem. 5 (4) (2013) 263.
[18] J. Lee, et al., Chem. Soc. Rev. 38 (5) (2009) 1450.
[19] B.Y. Xia, et al., Nat. Energy 1 (1) (2016) 15006.
[20] D. Farrusseng, et al., Angew. Chem. Int. Ed. 48 (41) (2009) 7502.
[21] J. Low, et al., Chem. Commun. 50 (74) (2014) 10768.
[22] K. Novoselov, Rev. Mod. Phys. 83 (3) (2011) 837.
[23] M.S. Dresselhaus, P.T. Araujo, Perspectives on the 2010 Nobel Prize in Physics for Graphene, ACS Publications, 2010.
[24] H. Liu, et al., J. Mater. Chem. 21 (10) (2011) 3335.
[25] S. Gilje, et al., Nano Lett. 7 (11) (2007) 3394.
[26] A. Rycerz, et al., Nat. Phys. 3 (3) (2007) 172.
[27] M. Katsnelson, et al., Nat. Phys. 2 (9) (2006) 620.
[28] D.A. Jasim, et al., 2D Mater. 3 (1) (2016), 014006.
[29] J.N. Gavgani, et al., Sens. Actuators B Chem. 229 (2016) 239.
[30] J.N. Gavgani, et al., RSC Adv. 5 (71) (2015) 57559.
[31] A. Hasani, et al., Phys. Status Solidi Rapid Res. Lett. 12 (5) (2018) 1870317.
[32] Y.R. Park, et al., Adv. Mater. Interfaces 4 (15) (2017) 1700476.
[33] F. Koppens, et al., Nat. Nanotechnol. 9 (10) (2014) 780.
[34] H. Wang, et al., IEEE Electron. Device Lett. 32 (9) (2011) 1209.
[35] F. Schwierz, Nat. Nanotechnol. 5 (7) (2010) 487.
[36] C. Zhang, et al., Nano Energy 2 (1) (2013) 88.
[37] N. Yang, et al., ACS Nano 7 (2) (2013) 1504.
[38] A. Mukherji, et al., ACS Nano 5 (5) (2011) 3483.
[39] Q. Han, et al., Talanta 101 (2012) 388.
[40] Y. Cao, et al., Nature 556 (7699) (2018) 43.
[41] S. Manzeli, et al., Nat. Rev. Mater. 2 (8) (2017) 17033.
[42] Y.-H. Wang, et al., Biosens. Bioelectron. 97 (2017) 305.
[43] B. You, et al., Phys. Chem. Chem. Phys. 18 (10) (2016) 7381.
[44] H. Li, et al., Acc. Chem. Res. 47 (4) (2014) 1067.
[45] R. Lv, et al., Acc. Chem. Res. 48 (1) (2014) 56.
[46] Y.H. Lee, et al., Adv. Mater. 24 (17) (2012) 2320.
[47] F. Wang, et al., Nanoscale 7 (47) (2015) 19764.
[48] M. Javaid, et al., Sci. Rep. 7 (1) (2017) 9775.
[49] T.P. Nguyen, et al., Electrochim. Acta 292 (2018) 136.
[50] H.I. Karunadasa, et al., Science 335 (6069) (2012) 698.
[51] M. Asadi, et al., Nat. Commun. 5 (1) (2014) 4470.
[52] F. Li, et al., Energy Environ. Sci. 9 (1) (2016) 216.
[53] M. Asadi, et al., Science 353 (6298) (2016) 467.
[54] N. Choudhary, et al., J. Mater. Res. 31 (7) (2016) 824.
[55] W. Choi, et al., Mater. Today 20 (3) (2017) 116.
[56] K. Zhang, et al., J. Mater. Chem. C 5 (46) (2017) 11992.
[57] X. Wu, et al., ACS Nano 6 (8) (2012) 7443.
[58] C. Grazianetti, et al., 2D Mater. 3 (1) (2016), 012001.
[59] Z. Ni, et al., Nano Lett. 12 (1) (2011) 113.
[60] B. Hoskins, R. Robson, J. Am. Chem. Soc. 112 (4) (1990) 1546.
[61] M. Eddaoudi, et al., Acc. Chem. Res. 34 (4) (2001) 319.
[62] M. O'Keeffe, et al., Acc. Chem. Res. 41 (12) (2008) 1782.
[63] H. Li, et al., Nature 402 (6759) (1999) 276.
[64] W. Xia, et al., Energy Environ. Sci. 8 (7) (2015) 1837.
[65] R. Antwi-Baah, H. Liu, Materials 11 (11) (2018) 2250.
[66] O.K. Farha, et al., J. Am. Chem. Soc. 134 (36) (2012) 15016.
[67] J. Liu, et al., Chem. Soc. Rev. 41 (6) (2012) 2308.
[68] H. Furukawa, et al., Science 329 (5990) (2010) 424.
[69] X.S. Wang, et al., Angew. Chem. Int. Ed. 47 (38) (2008) 7263.
[70] K. Koh, et al., J. Am. Chem. Soc. 131 (12) (2009) 4184.
[71] O.K. Farha, et al., Nat. Chem. 2 (11) (2010) 944.
[72] U. Stoeck, et al., Chem. Commun. 48 (88) (2012) 10841.
[73] H. Deng, et al., Science 336 (6084) (2012) 1018.
[74] S.S.-Y. Chui, et al., Science 283 (5405) (1999) 1148.
[75] G. Férey, et al., Angew. Chem. Int. Ed. 43 (46) (2004) 6296.
[76] S. Chavan, et al., Chem. Mater. 22 (16) (2010) 4602.
[77] B. Gomez-Lor, et al., Chem. Mater. 17 (10) (2005) 2568.
[78] Y. Fu, et al., Angew. Chem. Int. Ed. 51 (14) (2012) 3364.
[79] B. Hu, Aresta, A. Dibenedetto, A. Angelini, et al., J. CO2 Util. (2013), 3.
[80] J. Schneider, et al., Chem. Soc. Rev. 41 (6) (2012) 2036.
[81] B. Hu, et al., J. CO2 Util. 1 (2013) 18.
[82] Y. Hori, et al., J. Chem. Soc., Faraday Trans. 85 (8) (1989) 2309.
[83] R.J. Lim, et al., Catal. Today 233 (2014) 169.
[84] A.M. Appel, et al., Chem. Rev. 113 (8) (2013) 6621.
[85] L. Torrente-Murciano, et al., J. CO2 Util. 6 (2014) 34.
[86] J. Wu, et al., J. Power Sources 258 (2014) 189.
[87] E.E. Benson, et al., Chem. Soc. Rev. 38 (1) (2009) 89.
[88] N. García Rey, D.D. Dlott, J. Phys. Chem. C 119 (36) (2015) 20892.
[89] Z. Chen, et al., Proc. Natl. Acad. Sci. 109 (39) (2012) 15606.
[90] J. Qiao, et al., Chem. Soc. Rev. 43 (2) (2014) 631.
[91] J.A. Keith, E.A. Carter, J. Phys. Chem. Lett. 4 (23) (2013) 4058.
[92] K. Dhar, C. Cavallotti, J. Phys. Chem. A 118 (38) (2014) 8676.
[93] M. Karamad, et al., ACS Catal. 5 (7) (2015) 4075.
[94] Z. Liu, et al., J. CO2 Util. 15 (2016) 50.
[95] D. DeCiccio, et al., Electrochem. Commun. 52 (2015) 13.
[96] J. Rosen, et al., ACS Catal. 5 (8) (2015) 4586.
[97] Y. Hori, Electrochemical CO2 reduction on metal electrodes, in: C.G. Vayenas, et al. (Eds.), Modern Aspects of Electrochemistry, Springer New York, New York, NY, 2008, p. 89.

[98] J. Wu, et al., Adv. Sci. 4 (11) (2017) 1700194.
[99] Y. Garsany, et al., Experimental Methods for Quantifying the Activity of Platinum Electrocatalysts for the Oxygen Reduction Reaction, ACS Publications, 2010.
[100] J.R. Bolton, Science 202 (4369) (1978) 705.
[101] J.-M. Lehn, R. Ziessel, Proc. Natl. Acad. Sci. 79 (2) (1982) 701.
[102] C. Costentin, et al., Chem. Soc. Rev. 42 (6) (2013) 2423.
[103] J. Rosen, et al., ACS Catal. 5 (7) (2015) 4293.
[104] Q. Lu, et al., Nat. Commun. 5 (2014) 3242.
[105] S. Verma, et al., Phys. Chem. Chem. Phys. 18 (10) (2016) 7075.
[106] K. Jiang, et al., Energy Environ. Sci. 11 (4) (2018) 893.
[107] E. Barton Cole, et al., J. Am. Chem. Soc. 132 (33) (2010) 11539.
[108] M. Asadi, et al., Nat. Commun. 5 (2014) 4470.
[109] S. Lin, et al., Science 349 (6253) (2015) 1208.
[110] F. Li, et al., Energy Environ. Sci. 9 (1) (2016) 216.
[111] A. Murata, Y. Hori, Bull. Chem. Soc. Jpn. 64 (1) (1991) 123.
[112] K. Hara, et al., J. Electrochem. Soc. 141 (8) (1994) 2097.
[113] T.-Y. Chang, et al., Mater. Lett. 63 (12) (2009) 1001.
[114] O. Koga, Y. Hori, Electrochim. Acta 38 (10) (1993) 1391.
[115] S. Kaneco, et al., Electrochim. Acta 44 (4) (1998) 573.
[116] S. Kaneco, et al., Electrochemical reduction of CO2 on various metal electrodes in KOH plus methanol at ambient temperature and pressure, in: Abstracts of papers of the american chemical society, AMER chemical soc 1155 16TH ST, NW, Washington, DC 20036 USA, vol. 215, 1998, p. U406.
[117] K.P. Kuhl, et al., Energy Environ. Sci. 5 (5) (2012) 7050.
[118] Y. Qu, X. Duan, Chem. Soc. Rev. 42 (7) (2013) 2568.
[119] D. Gao, et al., J. Am. Chem. Soc. 137 (13) (2015) 4288.
[120] R. Reske, et al., J. Am. Chem. Soc. 136 (19) (2014) 6978.
[121] S. Back, et al., ACS Catal. 5 (9) (2015) 5089.
[122] H. Mistry, et al., J. Am. Chem. Soc. 136 (47) (2014) 16473.
[123] J.H. Koh, et al., J. Phys. Chem. C 119 (2) (2014) 883.
[124] A. Salehi-Khojin, et al., J. Phys. Chem. C 117 (4) (2013) 1627.
[125] A.S. Hall, et al., J. Am. Chem. Soc. 137 (47) (2015) 14834.
[126] W. Tang, et al., Phys. Chem. Chem. Phys. 14 (1) (2012) 76.
[127] Y.i. Hori, Electrochemical CO2 reduction on metal electrodes, in: Modern Aspects of Electrochemistry, Springer, 2008, p. 89.
[128] A. Schizodimou, G. Kyriacou, Electrochim. Acta 78 (2012) 171.
[129] K.W. Frese, J. Electrochem. Soc. 138 (11) (1991) 3338.
[130] C.W. Li, M.W. Kanan, J. Am. Chem. Soc. 134 (17) (2012) 7231.
[131] Y. Hori, et al., Electrochim. Acta 39 (11–12) (1994) 1833.
[132] Y. Chen, et al., J. Am. Chem. Soc. 134 (49) (2012) 19969.
[133] F. Lei, et al., Nat. Commun. 7 (2016) 12697.
[134] J. Wu, et al., J. Mater. Chem. 2 (6) (2014) 1647.
[135] D. Deng, et al., Nat. Nanotechnol. 11 (3) (2016) 218.
[136] H. Tao, et al., J. Mater. Chem. 5 (16) (2017) 7257.
[137] A.K. Geim, K.S. Novoselov, The rise of graphene, in: Nanoscience and Technology: a Collection of Reviews from Nature Journals, World Scientific, 2010, p. 11.
[138] X. Duan, et al., Adv. Mater. 29 (41) (2017) 1701784.
[139] S. Navalon, et al., Coord. Chem. Rev. 312 (2016) 99.
[140] C. Rogers, et al., J. Am. Chem. Soc. 139 (11) (2017) 4052.
[141] P. Su, et al., Small 12 (44) (2016) 6083.
[142] F. Li, et al., Nano Energy 31 (2017) 270.
[143] M. Zeng, Y. Li, J. Mater. Chem. 3 (29) (2015) 14942.
[144] X. Hong, et al., ACS Catal. 6 (7) (2016) 4428.
[145] K. Chan, et al., ChemCatChem 6 (7) (2014) 1899.
[146] Z.P. Jovanov, et al., J. Catal. 343 (2016) 215.
[147] P. Abbasi, et al., ACS Nano 11 (1) (2017) 453.
[148] R. Kas, et al., Nat. Commun. 7 (1) (2016) 10748.
[149] X. Feng, et al., J. Am. Chem. Soc. 137 (14) (2015) 4606.
[150] Q. Lu, et al., Nat. Commun. 5 (1) (2014) 3242.
[151] W. Zhu, et al., J. Am. Chem. Soc. 136 (46) (2014) 16132.
[152] K. Manthiram, et al., J. Am. Chem. Soc. 136 (38) (2014) 13319.
[153] J. Wu, et al., Nat. Commun. 7 (1) (2016) 13869.
[154] D.J. Tranchemontagne, et al., Chem. Soc. Rev. 38 (5) (2009) 1257.
[155] W. Lu, et al., Chem. Soc. Rev. 43 (16) (2014) 5561.
[156] Y. Bian, et al., Processes 6 (8) (2018) 122.
[157] W.-J. Li, et al., J. Mater. Chem. 4 (32) (2016) 12356.
[158] N.A. Khan, S.H. Jhung, Coord. Chem. Rev. 285 (2015) 11.
[159] L. Garzón-Tovar, et al., J. Mater. Chem. 3 (41) (2015) 20819.
[160] E. Haque, S.H. Jhung, Chem. Eng. J. 173 (3) (2011) 866.
[161] V.V.e. Butova, et al., Russ. Chem. Rev. 85 (3) (2016) 280.
[162] I. Luz, et al., Chem. Mater. 29 (22) (2017) 9628.
[163] S. Chaemchuen, et al., Chem. Soc. Rev. 42 (24) (2013) 9304.
[164] Z. Bao, et al., J. Colloid Interface Sci. 353 (2) (2011) 549.
[165] C.E. Wilmer, et al., Nat. Chem. 4 (2) (2012) 83.
[166] C.A. Trickett, et al., Nat. Rev. Mater. 2 (8) (2017) 17045.
[167] R. Hinogami, et al., ECS Electrochem. Lett. 1 (4) (2012) H17.
[168] N. Kornienko, et al., J. Am. Chem. Soc. 137 (44) (2015) 14129.
[169] R.S. Kumar, et al., Electrochem. Commun. 25 (2012) 70.
[170] M. Perfecto-Irigaray, et al., RSC Adv. 8 (38) (2018) 21092.
[171] X. Kang, et al., Chem. Sci. 7 (1) (2016) 266.
[172] Y. Wang, et al., ChemPhysChem 18 (22) (2017) 3142.
[173] L. Ye, et al., J. Mater. Chem. 4 (40) (2016) 15320.
[174] Y.-R. Wang, et al., Nat. Commun. 9 (1) (2018) 4466.
[175] Y. Guo, et al., J. Mater. Chem. 5 (47) (2017) 24867.
[176] X. Jiang, et al., J. Mater. Chem. 5 (36) (2017) 19371.
[177] T.N. Huan, et al., ACS Catal. 7 (3) (2017) 1520.
[178] Y. Ye, et al., Nano Energy 38 (2017) 281.
[179] D. Kim, et al., Nat. Commun. 5 (2014) 4948.
[180] X. Chen, et al., Catal. Sci. Technol. 5 (3) (2015) 1758.
[181] Q. Liu, et al., J. Am. Chem. Soc. 132 (41) (2010) 14385.
[182] H. Fujiwara, et al., Langmuir 14 (18) (1998) 5154.
[183] J.-Y. Liu, et al., Green Chem. 13 (8) (2011) 2029.
[184] Y. Li, et al., Carbon 99 (2016) 79.
[185] J. Ding, et al., Appl. Catal. B Environ. 202 (2017) 314.
[186] L. Cao, et al., J. Am. Chem. Soc. 133 (13) (2011) 4754.
[187] M.F. Kuehnel, et al., J. Am. Chem. Soc. 139 (21) (2017) 7217.
[188] L. Wang, T. Sasaki, Chem. Rev. 114 (19) (2014) 9455.
[189] X. Chen, et al., ACS Appl. Mater. Interfaces 4 (7) (2012) 3372.
[190] X. Chen, et al., Chem. Rev. 110 (11) (2010) 6503.
[191] B.R. Eggins, et al., J. Chem. Soc., Chem. Commun. (16) (1988) 1123.
[192] W. Tu, et al., Nanoscale 9 (26) (2017) 9065.
[193] A. Ali, W.-C. Oh, Sci. Rep. 7 (1) (2017) 1867.
[194] C. Wang, et al., J. Am. Chem. Soc. 133 (34) (2011) 13445.
[195] M. Wang, et al., Appl. Catal. B Environ. 183 (2016) 47.
[196] Y. Liu, et al., ACS Appl. Mater. Interfaces 5 (15) (2013) 7654.
[197] Q. Liu, et al., J. Mater. Chem. 1 (38) (2013) 11563.
[198] D. Sun, et al., Chemistry—A Eur. J. 20 (16) (2014) 4780.
[199] R. Li, et al., Adv. Mater. 26 (28) (2014) 4783.
[200] D. Sun, et al., Chem. Commun. 51 (11) (2015) 2056.
[201] Y. Lee, et al., Chem. Commun. 51 (92) (2015) 16549.
[202] S. Wang, X. Wang, Appl. Catal. B Environ. 162 (2015) 494.
[203] H.-Q. Xu, et al., J. Am. Chem. Soc. 137 (42) (2015) 13440.
[204] S. Yan, et al., J. Mater. Chem. 4 (39) (2016) 15126.
[205] N. Sadeghi, et al., J. CO2 Util. 16 (2016) 450.
[206] S. Goyal, et al., Catalysts 8 (12) (2018) 581.
[207] M. Chen, et al., Nanotechnology 29 (28) (2018) 284003.
[208] X. He, W.-N. Wang, J. Mater. Chem. 6 (3) (2018) 932.
[209] C. Chen, et al., Chem. Sci. 9 (47) (2018) 8890.
[210] M. Wang, et al., J. Mater. Chem. 6 (11) (2018) 4768.
[211] D. Sun, et al., Chemistry—A Eur. J. 19 (42) (2013) 14279.
[212] N. Sadeghi, et al., J. Mater. Chem. 6 (37) (2018) 18031.
[213] L. Ye, et al., Appl. Catal. B Environ. 227 (2018) 54.
[214] B. Han, et al., Angew. Chem. Int. Ed. 57 (51) (2018) 16811.
[215] A. Aijaz, et al., J. Am. Chem. Soc. 136 (19) (2014) 6790.
[216] Y. Li, et al., Nanoscale 10 (15) (2018) 7291.
[217] W. Zhang, et al., Adv. Sci. 5 (1) (2018) 1700275.